

Detailed homogeneous abundance studies of 14 Galactic *s*-process enriched post-AGB stars: In search of lead (Pb). * †

K. De Smedt¹, H. Van Winckel¹, D. Kamath¹, L. Siess², S. Goriely², A. I. Karakas³, and R. Manick¹

¹ Instituut voor Sterrenkunde, KU Leuven, Celestijnenlaan 200D, B-3001 Leuven, Belgium

² Institut d'Astronomie et d'Astrophysique, Université Libre de Bruxelles, ULB, CP 226, 1050 Brussels, Belgium

³ Research School of Astronomy and Astrophysics, Australian National University, Canberra, ACT 2611, Australia

Received / Accepted

ABSTRACT

Context. This paper is part of a larger project in which we systematically study the chemical abundances of Galactic and extragalactic post-asymptotic giant branch (post-AGB) stars.

Aims. Lead (Pb) is the final product of the *s*-process nucleosynthesis and is predicted to have large overabundances with respect to other *s*-process elements in AGB stars of low metallicities. However, Pb abundance studies of *s*-process enriched post-AGB stars in the Magellanic Clouds show a discrepancy between observed and predicted Pb abundances. The determined upper limits based on spectral studies are much lower than what is predicted.

Methods. We used high-resolution UVES and HERMES spectra for detailed spectral abundance studies of our sample of 14 Galactic post-AGB stars. None of the sample stars display clear Pb lines, and we only deduced upper limits of the Pb abundance by using spectrum synthesis in the spectral ranges of the strongest Pb lines.

Results. We do not find any clear evidence of Pb overabundances in our sample. The derived upper limits are strongly correlated with the effective temperature of the stars with increasing upper limits for increasing effective temperatures. We confirm the *s*-process enrichment and carbon enhancement of two unstudied 21 μm sources IRAS 13245-6428 and IRAS 14429-4539. The mildly *s*-process enhanced post-AGB star IRAS 17279-1119 is part of a binary system.

Conclusions. Stars with $T_{\text{eff}} > 7500$ K do not provide strong constraints on the Pb abundance. We conclude that the discrepancy between theory and observation increases towards lower metallicities. The model predictions are consistent with the deduced upper limits on the Pb abundances for all stars with $[\text{Fe}/\text{H}] > -0.7$ dex. For stars with $[\text{Fe}/\text{H}] < -0.7$ dex, however, the model predictions overestimate the Pb abundances with respect to the other *s*-process elements. All objects, except IRAS 17279-1119, confirm the relation between neutron exposure $[\text{hs}/\text{ls}]$ and third dredge-up efficiency $[\text{s}/\text{Fe}]$, whereas no relation between metallicity and neutron exposure is detected within the metallicity range of our total sample ($-1.4 < [\text{Fe}/\text{H}] < -0.2$). The mild enrichment of IRAS 17279-1119 can probably be attributed to a cut-off of the AGB evolution due to binary interactions. To our knowledge, IRAS 17279-1119 is the first *s*-process enhanced Galactic post-AGB star known in a binary system and is a possible precursor of the extrinsic Ba dwarf stars. Lead-rich stars have yet to be found in post-AGB stars.

Key words. Stars: AGB and post-AGB - (stars:) binaries: spectroscopic - Stars: abundances - Stars: evolution -

1. Introduction

The final evolution of low- to intermediate-mass single stars ($M \lesssim 7 M_{\odot}$) is characterised by a fast transition from the asymptotic giant branch (AGB) over the post-AGB track towards the planetary nebula phase. During late stages of AGB evolution, convective thermal pulses (TPs) occur in the intershell, which are possibly followed by third dredge-ups (TDUs) that transport newly synthesised material from the stellar interior to the surface. The main dredged-up element is ^{12}C as primary product of the triple alpha reaction. AGB stars are thought to be very im-

portant contributors to the total carbon and nitrogen enrichment of galaxies (e.g. Romano et al. 2010; Kobayashi et al. 2011).

Apart from ^{12}C , the TDU also brings elements created by neutron synthesis to the stellar surface. The slow-neutron capture process (or *s*-process) is at the origin of approximately half of all cosmic abundances past the iron peak. It is generally acknowledged that the $^{13}\text{C}(\alpha, n)^{16}\text{O}$ reaction is the main neutron source in low-mass AGB stars (1-3 M_{\odot}) (e.g. Straniero et al. 1995; Gallino et al. 1998; Mowlavi et al. 1998; Abia et al. 2002; Karakas & Lattanzio 2014; Neyskens et al. 2015). It is also widely accepted that a ^{13}C -pocket is produced by the transport of protons from the convective envelope into the He-rich intershell. The neutrons created in the ^{13}C -pocket by the alpha capture reaction can then be used for the creation of heavy elements by the slow neutron capture process (*s*-process). Although observations confirm that heavy elements can indeed be created by AGB stars, the physical mechanisms behind the AGB internal nucleosynthesis and associated dredge-up processes are poorly understood.

Along the valley of stability, the isotopes with the lowest cross-section for neutron capture are located around the nuclei with the magic number $N=50$ (the light *s*-elements or *ls*) and

Send offprint requests to: H. Van Winckel, Hans.VanWinckel@ster.kuleuven.be

* Based on observations collected with the Very Large Telescope at the ESO Paranal Observatory (Chili) of programme numbers 066.D-0171, 073.D-0241 and 094.D-0067.

† Based on observations made with the Mercator Telescope, operated on the island of La Palma by the Flemish Community, at the Spanish Observatorio del Roque de los Muchachos of the Instituto de Astrofísica de Canarias.

$N=80$ (the heavy s -elements or hs). The end product of the s -process nucleosynthesis chain is the doubly magic ^{208}Pb isotope. The ratio $[\text{hs}/\text{ls}]$ is an intrinsic indicator of the total neutron irradiation. The s -process chain is limited to the ls elements for moderate irradiations, while the hs elements are being produced for increasing neutron irradiation. When the neutron irradiation increases even further, the elements beyond the hs peak are produced up to the final product Pb. As the neutron production is thought to be largely independent of the initial metallicity, there are more neutrons available per iron seed and, hence at low metallicity Pb is predicted to have large overabundances with respect to other s -elements (see e.g. Gallino et al. 1998; Goriely & Mowlavi 2000; Lugaro et al. 2012, and references therein).

These Pb abundance predictions are confirmed in some low metallicity extrinsically enriched metal-poor objects, where strong Pb enhancements are indeed observed (e.g. Van Eck et al. 2001, 2003; Behara et al. 2010). These objects are polluted with matter from an evolved binary companion when it passed the TP-AGB phase but that is now a dim white dwarf. However, not all metal-deficient objects with s -process enrichment show this strong Pb overabundance (e.g. Aoki et al. 2001; Van Eck et al. 2003; Bisterzo et al. 2012). A very wide range of neutron irradiations are needed at a given metallicity to explain the abundance spread of extrinsically enhanced low metallicity objects (Bisterzo et al. 2010), the physical origin of which is not clear. A complicating factor in modelling the extrinsically enhanced objects is that the original enriched AGB star is now a cool white dwarf that is not detected.

Here we focus on intrinsically enriched objects. The AGB photospheres themselves are dominated by molecular transitions that hinder the study of individual elements (e.g. Abia et al. 2008). This problem does not occur in post-AGB stars, for which the photospheres are hotter and are dominated by atomic transitions. The spectra of post-AGB stars allow for extensive chemical studies of individual elements. Post-AGB atmospheres display the outcome of chemical enrichment from internal nucleosynthesis and dredge-up processes during the entire stellar evolution. This makes post-AGB stars ideal probes to study AGB nucleosynthesis (Van Winckel 2003).

In our recent studies of post-AGB stars in the Magellanic Clouds (van Aarle et al. 2011; Kamath et al. 2014, 2015), we focused on the intrinsic s -process enriched post-AGB star J004441.04-732136.4 (J004441) in the Small Magellanic Cloud (SMC; De Smedt et al. 2012, 2014). In De Smedt et al. (2014), we compared the observed abundance results with fine-tuned, theoretical state-of-the-art AGB models. Although this star is metal-poor and strongly s -process enriched, we found a strong discrepancy between the observed and predicted Pb overabundance. The best-fitting model overestimates the Pb overabundance by more than 2 dex. Moreover, the same Pb discrepancy was detected in three other metal-deficient post-AGB stars in the LMC (De Smedt et al. 2014). The extreme overabundances in combination with a negative $[\text{Pb}/\text{hs}]$ value may point to a neutron irradiation that is different from the currently accepted AGB s -process scenarios where the neutron irradiation occurs in the radiative layers of the intershell in between thermal pulses. One possible alternative is proton ingestion directly into the convective thermal pulse, but preliminary model calculations (Lugaro et al. 2015) are as yet inconclusive and not able to model the full abundance ratios of J004441.

This low Pb content was also detected by Reyniers et al. (2007a) for the LMC star MACHO 47.2496.8. For all of these objects with intrinsic enrichment, the upper limits of the Pb abundances are equal or smaller than the overabundances of

the other s -elements. In our most recent study (De Smedt et al. 2015), we found a similar discrepancy for two newly identified s -process enriched post-AGB stars in the LMC. We concluded that the low Pb abundance seems to be a common feature in s -process rich, post-AGB stars in the Magellanic Clouds. Furthermore, we find that all the objects studied until now have low initial masses and low metallicities. Therefore, the low observed Pb abundances strongly contradict theoretical nucleosynthetic predictions of Pb.

In this contribution, we extend our Pb studies and focus on Galactic s -process rich objects. We present a homogeneous study of the neutron irradiation as traced by the s -process element distribution of 14 post-AGB stars. We especially focus on the Pb abundances. In combination with the studied Magellanic Cloud objects, we aim at a systematic study of the distribution of s -elements detected in post-AGB stars, which cover a wide range of metallicities. We provide new constraints for the models of AGB nucleosynthesis and associated processes.

The selection of our Galactic sample stars and the observations are described in Sect. 2. The spectral analyses are discussed in Sect. 3 followed by the abundance results of all elements lighter than Pb in Sect. 4. The abundance results of Pb are presented in Sect. 5. The neutron irradiation of our sample of stars is discussed in Sect. 6. In Sect. 7, we specifically focus on the evolutionary status of one of the sample stars, IRAS 17279-1119. We end this paper with the conclusions in Sect. 8.

2. Sample selection and observations

Our sample consists of 12 Galactic post-AGB stars, which are known to be s -process rich, and two new post-AGB candidates, IRAS 13245-5036 and IRAS 14429-4539, for which no abundance studies have been reported yet. The majority of the already studied Galactic post-AGB stars are $21\ \mu\text{m}$ objects, named for the strong solid-state feature at $21\ \mu\text{m}$ (Kwok et al. 1989). To date, all $21\ \mu\text{m}$ objects are acknowledged to be post-AGB stars with carbon and s -process enhancements in their photospheres (e.g. Hrivnak et al. 2009). Since both IRAS 13245-5036 and IRAS 14429-4539 are post-AGB candidates with a clear $21\ \mu\text{m}$ feature (Cerrigone et al. 2011), we added these stars to our sample.

We use high-resolution spectra of two different spectrographs. The first spectrograph is the Ultraviolet and Visual Echelle Spectrograph (UVES; Dekker et al. (2000)), the echelle spectrograph mounted on the 8m UT2 Keuyen Telescope of the VLT array at the Paranal Observatory of ESO in Chili. The second spectrograph is the High Efficiency and Resolution Mercator Echelle Spectrograph (HERMES; Raskin et al. 2011), the spectrograph mounted on the 1.2m Mercator telescope at the Roque de los Muchachos Observatory on La Palma.

For all objects, we first checked whether optical high-resolution spectra with sufficient signal-to-noise (S/N) around $4058\ \text{\AA}$, the spectral region of the strongest identified Pb I line, were already available for UVES in the ESO archive and for HERMES in the archive of the Institute of Astronomy (KULeuven). If not, we requested and performed observations for those objects for which a S/N of 25 around $4058\ \text{\AA}$ would be reached within an hour. All objects, observational details and previous abundance studies are listed in Table 1. The last column shows the radial velocity of the observed spectra.

Table 1. Overview of the sample: name(s), observational logs, references of previous studies, and radial velocities.

IRAS	Other name	Date	UT start	Exp. time ^a (s)	Telescope+ Spectrograph	References	r_v (km/s)
05113+1347 ^d		2014-10-07	07:55	Blue: 1 × 2676	VLT + UVES	1	6 ± 2
		2014-11-23	05:03	Blue: 1 × 2676	VLT + UVES		5 ± 1
				Red: 2 × 1200	VLT + UVES		5 ± 1
05341+0852 ^d		2014-10-06	07:52	All: 1 × 1826	VLT + UVES	2	28 ± 1
		2014-10-06	08:28	All: 1 × 1826	VLT + UVES		28 ± 1
06530-0213		2014-12-24	04:03	All: 1 × 2427	VLT + UVES	3	52 ± 1
		2014-12-24	04:50	All: 1 × 2427	VLT + UVES		52 ± 1
07134+1005 ^d	HD 56126	2014-09-05	05:50	1 × 920	Mercator + HERMES	2	92 ± 1
		2014-09-08	05:39	1 × 1000	Mercator + HERMES		94 ± 1
07430+1115		2014-12-24	05:33	Blue: 1 × 2176	VLT + UVES	4	41 ± 2
				Red: 2 × 1000	VLT + UVES		41 ± 1
08143-4406 ^b		2001-01-16	06:41	Blue437: 2 × 1800	VLT + UVES	3	52 ± 2
		2001-01-16	07:16	Red860: 3 × 500	VLT + UVES		52 ± 1
		2001-02-01	04:21	Red: 1 × 1800	VLT + UVES		52 ± 1
08281-4850		2015-01-25	04:18	All: 1 × 2400	VLT + UVES	5	117 ± 1
		2015-01-25	03:47	All: 1 × 2600	VLT + UVES		116 ± 1
		2015-01-31	02:39	All: 1 × 2116	VLT + UVES		117 ± 1
13245-5036 ^d		2015-03-06	04:53	All: 1 × 346	VLT + UVES		54 ± 1
14325-6428 ^c		2004-05-13	07:13	Blue437: 1 × 1800	VLT + UVES	5	-83 ± 1
			Red860: 1 × 1800	VLT + UVES	-83 ± 1		
		06:39	Red: 1 × 1800	VLT + UVES	-82 ± 1		
14429-4539 ^{b,d}		2001-02-03	08:24	Red: 1 × 1800	VLT + UVES		0 ± 2
			08:55	Red: 1 × 1200	VLT + UVES		0 ± 2
		2001-02-06	07:53	Red: 1 × 1800	VLT + UVES		0 ± 2
		2001-02-12	07:54	Blue437: 3 × 2000	VLT + UVES		4 ± 2
			Red860: 3 × 2000	VLT + UVES	4 ± 2		
17279-1119	HD158616	2014-09-18	00:00	All: 1 × 65	VLT + UVES	6	62 ± 1
19500-1709 ^d	HD187885	2009-07-16	00:20	2 × 2000	Mercator + HERMES	2	15 ± 1
22223+4327 ^d	V448 Lac	2009-07-31	02:50	4 × 1800	Mercator + HERMES	2,6	-41 ± 1
22272+5435 ^d	HD235858	2014-08-29	01:55	3 × 720	Mercator + HERMES	1	-38 ± 1

¹Reddy et al. (2002), ²Van Winckel & Reyniers (2000), ³Reyniers et al. (2004), ⁴Reddy et al. (1999), ⁵Reyniers et al. (2007b), ⁶Rao et al. (2012)

^a Exposure times of UVES spectra are split up into three categories: exposure times for the Blue arm, Red arm, or both arms; the latter is indicated with 'All'. Terms 'Blue' and 'Red' refer to observations with the Blue390 and Red580 setting. For older observations, the Blue437 and Red860 settings have also been used.

^b For more information about these observations, see Reyniers (2002).

^c For more information about the observations of IRAS 14325-6428, see Reyniers et al. (2007b).

^d Identified 21 μ m source.

2.1. UVES spectra

The UVES spectra obtained in the period 2014–2015 (see Table 1) were observed using the same setting. We selected the dichroic beam splitter resulting in a wavelength coverage for the blue UVES arm from approximately 3280 to 4530 Å, and for the lower and upper part of the mosaic CCD chip from approximately 4780 to 5770 Å and from 5800 to 6810 Å, respectively. A slit width of 1 arcsecond was used to gain an optimal compromise between spectral resolution and slit-loss minimisation.

We used the reduced UVES spectra from Reyniers et al. (2004) for our analysis for IRAS 08143-4406. These spectra were observed with different settings, resulting in two sets of spectra representing different wavelength coverages. There is a time gap of 16 days between the observations of both sets of data. This gap was large enough to observe significant changes in the photosphere of IRAS 08143-4406, resulting in two different sets of atmospheric parameters in the analysis by Reyniers et al. (2004). The UVES spectra of post-AGB candidate IRAS 14429-4539 were obtained using the same settings as for IRAS 08143-

4406. For details about the observations of IRAS 08143-4406 and IRAS 14429-4539, we refer to Reyniers (2002). For IRAS 14325-6428, we use the observed spectra described in Reyniers et al. (2007b) for the spectral analysis.

All UVES spectra in Table 1, except for IRAS 08143-4406 and IRAS 14429-4539, were reduced using the UVES pipeline in the Reflex environment of ESO ¹. The reduction scheme includes extraction of frames, determinations of wavelength calibration and applying this scale to flat-field divided data. Cosmic clipping was also included. We chose the standard reduction parameters of the UVES pipeline as these gave the best signal-to-noise (S/N) ratio of the final spectrum. The spectra of IRAS 08143-4406 and IRAS 14429-4539 were already reduced with older versions of the UVES pipeline.

¹ <https://www.eso.org/sci/software/reflex/>

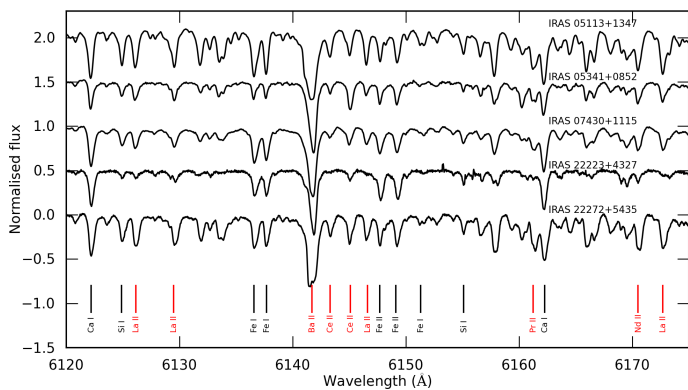


Fig. 1. Comparison of the normalised spectra of all sample stars with $T_{\text{eff}} < 7000$ K. The spectra have been shifted in flux for clarity and all spectra are shifted to zero velocity. Red and black vertical lines indicate positions of s nuclei and non s nuclei, respectively. For more information, see text.

2.2. HERMES spectra

All HERMES spectra were obtained in high-resolution mode ($\lambda/\Delta\lambda = 85,000$). These spectra cover a wavelength range from about 3770 Å up to about 9000 Å, although some gaps in the spectra are present at large wavelengths, as the reddest orders are too long for the CCD. The specific reduction pipeline of HERMES (Raskin et al. 2011) includes similar steps as the UVES pipeline and is used for the full reduction of the spectra.

2.3. Normalisation and merging

When necessary, the individual reduced spectra of each object are first corrected for radial velocity differences (see Table 1). The radial velocities are determined for UVES spectra using the positions of individual spectral lines. The radial velocities are determined for HERMES spectra using a cross-correlation routine specific to the HERMES pipeline (Raskin et al. 2011).

Thereafter, weighted mean spectra are calculated for the individual wavelength ranges of UVES and for the total HERMES spectra. For the normalisation of the spectra, we subdivided the weighted mean spectra into fixed wavelength ranges of 120 Å where the first and last 10 Å overlap with the previous and subsequent spectral parts. Specific care was taken to conserve the Balmer profiles during the normalisation procedure. Each subspectrum is normalised individually by fitting a fifth order polynomial through interactively defined continuum points. After the individual normalisations, all normalised subspectra are then merged into one large spectrum, which is used for the spectral abundance studies.

3. Spectral analyses

Figs. 1, 2, and 3 presents the spectral region around the Ba II line at 6141.813 Å together with the identification of several spectral lines. Each figure corresponds to a different range in effective temperature T_{eff} (see Sect. 3.1). Fig. 1 shows our sample stars with $T_{\text{eff}} < 7000$ K, Fig. 2 shows sample stars with $7000 \text{ K} \leq T_{\text{eff}} < 8000$ K, and Fig. 3 shows the sample stars with $T_{\text{eff}} \geq 8000$ K. The figures illustrate how the number of strong spectral lines decreases with increasing effective temperature for all elements.

The overall S/N of the red spectra of UVES (see Table 1) and the optical spectral regions of HERMES is very high and ranges from 80 to 200. We perform a comparative systematic analysis

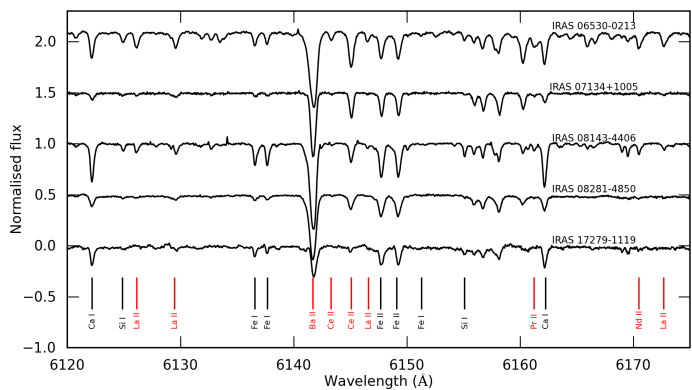


Fig. 2. Similar to Fig. 1, except for the sample stars with $7000 \text{ K} \leq T_{\text{eff}} < 8000$ K.

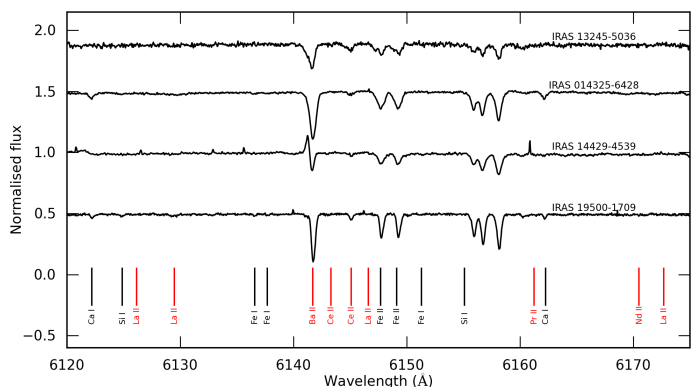


Fig. 3. Similar to Figs. 1 and 2, except for the sample stars with $T_{\text{eff}} \geq 8000$ K.

of all objects and hence decide not to rely on the previous results in the literature, but perform an independent full spectral analysis using the same method for all objects. Depending on the temperature of the star, the S/N of spectra below 3700 Å are too poor for both spectrographs, so these regions are not used for our analysis. For the UVES data, we use the full red spectral region sampled in our setting as well as the spectral region from 3900 Å redwards. For hotter stars, we could extend this region towards bluer wavelengths.

In this contribution we focus on Pb but unfortunately, the optical spectrum of Pb is poor in spectral lines for the typical atmospheric parameters of our sample stars. The strongest Pb I lies in the blue part of the spectrum ($\lambda 4057.807$ Å), a spectral region with low S/N and a large number of blends. For some hotter stars, the strongest line of Pb II at 5608.853 Å is used to constrain the Pb abundance. To investigate the possible strength of Pb, we calculated which input [Pb/H] abundance is needed to create a spectral line of 5 mÅ. This value is the lower limit for distinguishing spectral lines from noise in the spectra. Fig. 4 shows these theoretical Pb abundances for different effective temperatures and for $[\text{Fe}/\text{H}] = -1.0$ dex and $[\text{Fe}/\text{H}] = -0.2$ dex. These abundances are calculated for a $\log g = 1.5$ dex for all stars with $T_{\text{eff}} < 9250$ K and for $\log g = 2.0$ dex for 9250 and 9500 K. Fig. 4 shows that the needed Pb abundance for a spectral line detection increases significantly with rising temperature. The figure also shows that the effect of metallicity is negligible in the temperature and metallicity range of the programme stars.

In order to trace Pb we have to synthesise the spectral regions around the Pb lines and, hence, we need a complete set of abundances. For these, we used the spectral regions with good

Table 2. Model atmospheres of the sample of stars. The errors for [Fe/H] include line-to-line scatter and model uncertainty (see Sect. 3.2). N_{FeI} and N_{FeII} show the number of lines used for Fe I and Fe II, respectively.

Object	T_{eff} (K) ± 125	$\log g$ (dex) ± 0.25	ξ_t (km/s) ± 0.25	[FeI/H]	[FeII/H]	N_{FeI}	N_{FeII}
IRAS 05113+1347	5500	0.50	5.00	-0.49 ± 0.15	-0.54 ± 0.17	21	11
IRAS 05341+0852	6750	1.25	3.50	-0.70 ± 0.15	-0.54 ± 0.11	47	20
IRAS 06530-0213	7375	1.25	4.00	-0.38 ± 0.20	-0.32 ± 0.11	24	54
IRAS 07134+1005	7250	0.50	3.25	-0.96 ± 0.31	-0.91 ± 0.20	42	32
IRAS 07430+1115	6000	1.00	3.25	-0.31 ± 0.15	-0.35 ± 0.15	43	17
IRAS 08143-4406 ^a	7000	1.50	5.50	-0.45 ± 0.16	-0.43 ± 0.11	17	8
IRAS 08143-4406 ^b	7250	1.50	5.00	-0.37 ± 0.17	-0.36 ± 0.11	70	23
IRAS 08281-4850	7875	1.25	5.50	-0.29 ± 0.31	-0.26 ± 0.11	44	23
IRAS 13245-5036	9500	2.75	4.50	-0.35 ± 0.20	-0.30 ± 0.10	21	41
IRAS 14325-6428	8000	1.00	5.75	-0.55 ± 0.33	-0.56 ± 0.10	26	58
IRAS 14429-4539	9375	2.50	4.75	-0.26 ± 0.21	-0.18 ± 0.11	26	52
IRAS 17279-1119	7250	1.25	3.00	-0.51 ± 0.19	-0.64 ± 0.12	44	30
IRAS 19500-1709	8000	1.00	6.00	-0.58 ± 0.42	-0.59 ± 0.10	33	32
IRAS 22223+4327	6500	1.00	4.75	-0.32 ± 0.14	-0.30 ± 0.11	80	25
IRAS 22272+5435	5750	0.50	4.25	-0.77 ± 0.14	-0.77 ± 0.12	35	24

^a Results of the Blue437 and Red860 observations of IRAS 08143-4406 in Table 1.

^b Results of the Red580 observations of IRAS 08143-4406 in Table 1.

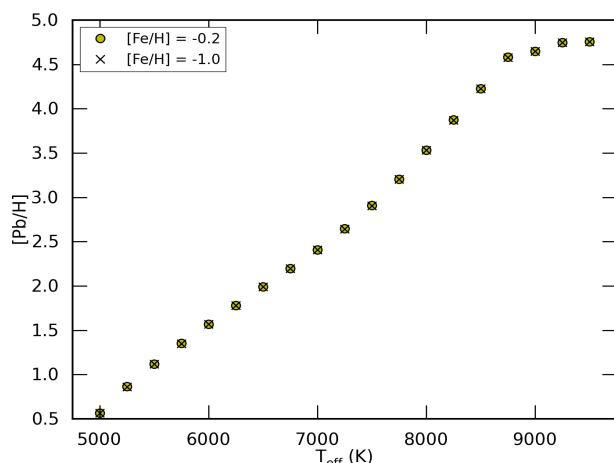


Fig. 4. [Pb/H] abundance needed to obtain a Pb I or Pb II spectral line of 5 mÅ as a function of effective temperature T_{eff} and metallicity [Fe/H]. For more information, see text.

S/N. We use the same methods for the atmospheric parameter determinations and abundance studies for all programme stars. Then, we used these abundances to make detailed spectral synthesis spectra in the regions of the strongest Pb lines. In this way, we obtained the best constraints on the Pb abundances.

We have written a Python wrapper (PyMOOG) around the local thermal equilibrium (LTE) abundance calculation routine MOOG (version June 2014 Sneden 1973), which is combined with LTE Kurucz-Castelli atmosphere models (Castelli & Kurucz 2004). Spectral line identification is based on linelists from the Vienna atomic line database (VALD) (Kupka et al. 1999) in combination with a list of spectral lines gathered at the Institute of Astronomy (KULeuven) for the chemical analysis of A, F, and G stars (Van Winckel & Reyniers 2000). The implemented linelists cover a wavelength range from 3000 up to 11000 Å, covering the full wavelength coverage of the UVES and HERMES spectra. We included linelists for about 160 ions, ranging from helium (He, $Z=2$) up to uranium (U, $Z=92$). Neutral and firstly ionised lines are available for most elements. For some *s*-

elements, the second ionisation is also included and is used for the spectral abundance studies of the hottest stars in the sample.

The equivalent width (EW) of spectral lines are interactively measured via direct integration in PyMOOG. The abundances are computed via an iterative process in which the theoretical EWs of single lines are computed for given abundances and matched to the observed EWs. Blended lines are avoided as much as possible, although for some species, Pb in particular, we sometimes could only use blended lines in our strongly *s*-process enriched stars.

3.1. Atmospheric parameters

The atmospheric parameters are determined using Fe I and Fe II lines in the standard spectroscopic method: the effective temperature T_{eff} is determined by imposing the iron abundance to be independent of lower excitation potential; surface gravity $\log g$ by imposing ionisation equilibrium between the individual Fe I and Fe II abundances; microturbulent velocity by imposing the iron abundance to be independent of reduced equivalent width, which we define as EW/λ .

To decrease the abundance uncertainty imposed by the step size of the atmospheric parameters, we use linear interpolation to calculate atmospheric models that lie within the parameter steps of the Kurucz-Castelli models. We choose temperature steps of 125 K, surface gravity steps of 0.25 dex, and microturbulent velocity steps of 0.25 km/s.

The individual atmospheric parameter results for the sample of stars are listed in Table 2. The shown uncertainties for [FeI/H] and [FeII/H] include both line-to-line scatter and atmospheric parameter uncertainties as described below in Sect. 3.2. Similar to Reyniers et al. (2004), we have determined the atmospheric parameters separately for the different spectra sets of IRAS 08143-4406 (see Sect. 2). Within the time gap between the observations, the spectral lines of IRAS 08143-4406 had changed significantly, resulting in different sets of atmospheric parameters. These changing spectral line shapes are expected as post-AGB stars cross the Population II Cepheid instability strip during their evolution, and, hence, pulsations may strongly change the atmospheric parameters. For the other stars, the spec-

tral lines did not show any visible changes within the time of the observations.

Typically, the uncertainties for Fe I lines are larger than those of Fe II because of the larger sensitivity of Fe I lines to temperature. For the two new 21 μm post-AGB stars IRAS 13245-5036 and IRAS 14429-4539, we find higher temperatures and higher surface gravities with respect to the other sample stars, which points to a more evolved phase of the post-AGB evolutionary stage.

3.2. Abundance determination

The abundance analysis of the individual programme star is performed with our preferred atmospheric parameter sets listed in Table 2. We only use spectral lines with EWs smaller than 150 mÅ, as stronger lines are saturated. We also avoid spectral lines with EWs smaller than 5 mÅ as these may be confused with noise in the spectra.

Ideally, we would only use isolated lines but the strong enrichments and/or high metallicities of the programme stars make this difficult. Therefore, we use spectrum synthesis to check if suspicious spectral lines are part of identified blends. For some elements, we could only determine the abundance with spectral synthesis.

The number of spectral lines for the carbon abundance determination varies strongly with temperature, while for oxygen only a limited number of spectral lines is available in the temperature range of the programme stars. For almost all stars, the O abundances are determined from the high excitation oxygen multiplet at 6156 Å and/or the forbidden oxygen lines at 6300 and 6363 Å. These lines are not affected by possible non-LTE effects (see e.g. Kiselman 2002). For some stars with HERMES spectra, we could determine the nitrogen abundances for spectral lines in the wavelength range between 7000 and 9000 Å. These lines are known to be non-LTE sensitive, however, and therefore we apply the temperature-sensitive, non-LTE corrections of Lyubimkov et al. (2011) (see Sect. 4).

The number of lines available for elements ranging from sodium (Na, $Z=11$) up to sulphur (S, $Z=16$) is limited. Therefore, these abundances cannot be determined in all stars. For the iron-peak elements, ranging from calcium (Ca, $Z=20$) up to zinc (Zn, $Z=30$), we find a wide range of elemental abundances for the majority of stars.

In all programme stars, we find spectral lines of *s*-process elements of the strontium peak (Sr, $Z=38$) and barium peak (Ba, $Z=56$), respectively known as the light *s*-process (ls) elements and heavy *s*-process (hs) elements. Unfortunately, we could not determine the abundance of Sr in any object as the available Sr lines are always strongly saturated. For the other ls elements yttrium (Y, $Z=39$) and zirconium (Zr, $Z=40$), we find useful spectral lines in each object to determine their abundance. For some stars, we also detect one or two lines for molybdenum (Mo, $Z=42$).

For the hs elements, we can always determine the abundances of lanthanum (La, $Z=57$) and neodymium (Nd, $Z=60$), and for most of the stars, strong cerium (Ce, $Z=58$) lines are present. In a few objects, we are able to determine the abundance of Ba with a weak Ba II line. In the other stars, the available Ba lines are highly saturated. We can also determine the abundances of a range of elements beyond the Ba-peak such as europium (Eu, $Z=63$), gadolinium (Gd, $Z=64$), dysprosium (Dy, $Z=66$), erbium (Er, $Z=68$), ytterbium (Yb, $Z=70$), lutetium (Lu, $Z=71$), hafnium (Hf, $Z=72$), and tungsten (W, $Z=74$). Most of

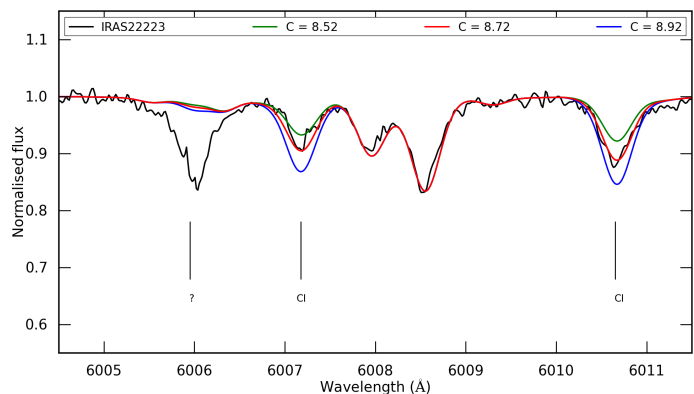


Fig. 5. Spectrum synthesis of the C I lines at 6007.176 and 6010.675 Å for IRAS 22223+4327. The black spectrum is the observed HERMES spectrum; the coloured spectra represent synthetic spectra with different C abundances. The red line represents the determined C abundance; the green and blue spectra represent synthetic spectra with a C abundance of -0.2 dex and +0.2 dex, respectively.

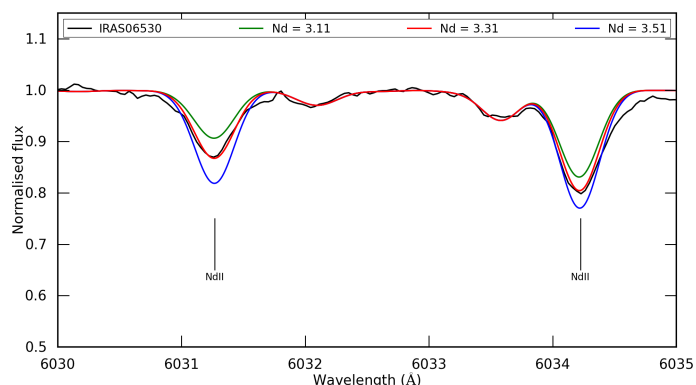


Fig. 6. Spectrum synthesis of the Nd II lines at 6031.270 and 6034.228 Å for IRAS 06530-0213. The black spectrum is the observed UVES spectrum; the coloured spectra represent synthetic spectra with different Nd abundances. The red line represents the determined Nd abundance; the green and blue spectra represent synthetic spectra with a Nd abundance of -0.2 dex and +0.2 dex, respectively.

the abundances of these elements are determined with spectral synthesis. We present here a very homogeneous determination of these very heavy elements in all objects with the same atomic data and methodology. Despite the fact that the abundances are often determined with only one or a few lines, we consider the abundances reliable. The high abundances are a clear indication that several elements beyond the Ba-peak are also efficiently synthesised in these objects.

4. Abundance results to $Z < 82$ for all sample stars

The abundance results of the different programme stars are listed in Tables 3 to 6; each table contains stars of similar effective temperatures. The corresponding $[X/\text{Fe}]$ results are plotted in Figs. 8, 9, and 10. An overview of the lines used for these analyses can be found in 15 catalogues available at CDS². The abundance results for Pb are discussed in Sect. 5.

The total errors σ_{tot} in Tables 3 to 6 are calculated following the methodology of Deroo et al. (2005). The errors due to atmospheric parameter uncertainties are calculated by determining the elemental abundances for atmospheric models with an

² A link to the catalogues

Table 3. Abundance results of IRAS 05113+1347, IRAS 05341+0852, IRAS 07430+1115, and IRAS 22272+5435.

Ion	log ϵ_{\odot}	IRAS05113 [Fe/H] = -0.49 $T_{\text{eff}} = 5500$ K log $g = 0.5$ dex					IRAS05341 [Fe/H] = -0.54 $T_{\text{eff}} = 6750$ K log $g = 1.25$ dex					IRAS07430 [Fe/H] = -0.31 $T_{\text{eff}} = 6000$ K log $g = 1.00$ dex					IRAS22272 [Fe/H] = -0.77 $T_{\text{eff}} = 5750$ K log $g = 0.5$ dex				
		N	log ϵ	σ_{121}	[X/Fe]	σ_{tot}	N	log ϵ	σ_{121}	[X/Fe]	σ_{tot}	N	log ϵ	σ_{121}	[X/Fe]	σ_{tot}	N	log ϵ	σ_{121}	[X/Fe]	σ_{tot}
C I	8.43	6	8.87	0.11	0.65	0.16	16	8.73	0.10	1.03	0.10	6	8.87	0.06	0.79	0.13	14	8.71	0.07	1.05	0.12
O I	8.69	1	8.49	0.20	0.01	0.27	2	8.71	0.07	0.75	0.11	2	8.64	0.20	0.30	0.22	2	8.55	0.02	0.63	0.09
Na I	6.24	2	5.88	0.01	0.17	0.12	1	6.00	0.20	0.46	0.23	2	6.20	0.09	0.27	0.12	2	5.90	0.00	0.42	0.09
Mg I	7.60	1	7.20	0.20	0.13	0.24	1	6.88	0.20	-0.02	0.24	2	7.26	0.01	-0.03	0.11	3	6.75	0.20	-0.08	0.17
Al I	6.45											2	6.37	0.13	0.24	0.15	1	6.07	0.20	0.39	0.23
Si I	7.51	4	7.23	0.06	-0.07	0.20	5	7.04	0.10	0.26	0.18	5	7.52	0.13	0.36	0.19	4	7.06	0.05	0.32	0.16
S I	7.12	1	6.97	0.20	0.06	0.25	3	6.65	0.09	0.25	0.15	2	6.69	0.02	-0.08	0.13	2	6.64	0.02	0.28	0.11
Ca I	6.34	3	5.66	0.03	-0.14	0.10	7	5.83	0.05	0.20	0.08	7	6.03	0.09	-0.0	0.08	8	5.81	0.10	0.24	0.08
Ca II	6.34						3	5.97	0.09	0.36	0.12						1	5.79	0.20	0.22	0.24
Sc II	3.15	6	2.87	0.09	-0.08	0.13	6	2.72	0.09	0.30	0.09	4	3.00	0.06	0.20	0.10	3	2.75	0.20	0.37	0.18
Ti I	4.95	4	4.47	0.09	0.05	0.13						5	4.90	0.11	0.27	0.11	2	4.50	0.05	0.32	0.10
Ti II	4.95	3	4.41	0.05	-0.34	0.12	2	4.50	0.20	0.28	0.19	9	4.86	0.09	0.26	0.09	2	4.47	0.03	0.29	0.11
V I	3.93	3	3.71	0.11	0.32	0.15						1	4.00	0.20	0.38	0.24					
V II	3.93											2	3.99	0.03	0.41	0.13	2	3.21	0.03	0.05	0.11
Cr I	5.64	4	5.02	0.03	-0.09	0.10	2	4.99	0.06	0.05	0.12	2	5.20	0.02	-0.13	0.09	4	4.91	0.06	0.03	0.08
Cr II	5.64						10	5.03	0.06	0.12	0.07	6	5.16	0.07	-0.13	0.08	9	4.94	0.06	0.06	0.07
Mn I	5.43	1	4.60	0.20	-0.3	0.24						2	4.96	0.06	-0.15	0.11	1	4.58	0.20	-0.08	0.22
Mn II	5.43						1	5.40	0.20	0.70	0.22						1	4.60	0.20	-0.06	0.22
Fe I	7.50	21	6.96	0.11	0.00	0.08	47	6.80	0.10	0.00	0.06	43	7.19	0.08	0.00	0.05	35	6.73	0.07	0.00	0.05
Fe II	7.50	10	7.29	0.13	0.00	0.11	20	6.77	0.07	0.00	0.05	17	7.15	0.08	0.00	0.06	24	6.73	0.08	0.00	0.05
Co I	4.99	2	4.59	0.01	0.13	0.13															
Ni I	6.22	5	5.78	0.10	0.10	0.11	6	5.81	0.06	0.29	0.08	11	5.89	0.12	-0.01	0.09	8	5.66	0.07	0.21	0.07
Cu I	4.19	1	3.94	0.20	0.28	0.24	1	4.25	0.20	0.76	0.23	2	3.92	0.07	0.05	0.12	1	3.80	0.20	0.37	0.22
Zn I	4.56	1	4.15	0.20	-0.2	0.32						1	4.46	0.20	0.25	0.28	1	4.06	0.20	0.27	0.29
Y II	2.21	2	3.30	0.20	1.29	0.22	4	3.47	0.10	1.98	0.12	1	3.25	0.20	1.39	0.24	4	3.14	0.08	1.69	0.12
Zr II	2.58	3	3.73	0.11	1.36	0.15	2	3.61	0.06	1.76	0.10	2	3.45	0.12	1.22	0.15	3	3.35	0.08	1.54	0.11
La II	1.10	6	2.69	0.16	1.80	0.16	8	2.82	0.08	2.45	0.11	11	2.50	0.12	1.75	0.12	6	2.65	0.20	2.32	0.15
Ce II	1.58	4	3.18	0.10	1.80	0.14	5	3.12	0.06	2.27	0.10	5	2.71	0.09	1.47	0.11	4	2.66	0.06	1.84	0.11
Pr II	0.72	6	2.20	0.14	1.68	0.16	7	2.27	0.09	2.28	0.14	11	1.94	0.13	1.57	0.14	13	1.81	0.07	1.86	0.13
Nd II	1.42	8	2.88	0.05	1.66	0.13	23	3.18	0.11	2.49	0.13	17	2.64	0.08	1.57	0.12	7	2.61	0.05	1.96	0.13
Sm II	0.96	3	2.10	0.09	1.34	0.16	2	1.99	0.12	1.76	0.16	4	2.05	0.13	1.43	0.15	3	1.67	0.09	1.47	0.14
Eu II	0.52	2	1.21	0.10	0.90	0.16	2	1.25	0.09	1.46	0.14	2	0.98	0.07	0.81	0.13	2	0.89	0.06	1.14	0.12
Gd II	1.07	3	2.29	0.09	1.43	0.16	2	2.17	0.08	1.82	0.12	3	2.00	0.07	1.28	0.13	13	1.99	0.12	1.69	0.16
Tb II	0.30											1	1.70	0.20	1.75	0.27					
Dy II	1.10	2	2.34	0.01	1.44	0.14	2	2.25	0.20	1.88	0.20	2	2.18	0.00	1.43	0.13	8	2.13	0.09	1.80	0.11
Er II	0.92	4	2.15	0.07	1.43	0.14	2	2.23	0.05	2.04	0.12					3	1.74	0.04	1.58	0.10	
Yb II	0.84						1	2.50	0.20	2.39	0.24					1	2.00	0.20	1.93	0.24	
Lu II	0.10	2	1.34	0.20	1.45	0.23	2	1.74	0.01	2.36	0.12	1	0.85	0.20	1.10	0.25	2	1.25	0.20	1.92	0.21
Hf II	0.85	2	2.19	0.09	1.55	0.16	1	2.15	0.20	2.02	0.23					2	1.85	0.20	1.77	0.19	
W II	0.85						1	3.07	0.20	2.95	0.25					1	2.30	0.20	2.21	0.25	

Notes: For each ion, the table lists the used number of lines (N) for the abundance determination, the determined abundance (log ϵ), the uncertainty on this abundance due to line-to-line scatter (σ_{121}), the element over iron ratio ([X/Fe]) and the total uncertainty on [X/Fe] (σ_{tot}) which includes line-to-line scatter and atmospheric parameter uncertainty (see text for details).

The solar abundances (log ϵ_{\odot}) in the second column are retrieved from Asplund et al. (2009).

For all elemental abundances determined via only one spectral line or via spectrum synthesis, we adopt a line-to-line scatter of 0.20 dex.

effective temperature $T_{\text{eff}} \pm 125$ K, surface gravity log $g \pm 0.25$ dex and microturbulent velocity $\xi_t \pm 0.25$ km/s with respect to the preferred value. We include microturbulent velocity in our error analysis despite the fact that for most ions, the associated error is only of the order of a few 0.01 dex. However, for some ions for which only relatively strong spectral lines are available like Y II, the error due to microturbulence can increase to about 0.1 dex.

The total uncertainty σ_{tot} on [X/Fe] is then the quadratic sum of the error on the mean (the line-to-line scatter σ_{121} divided by the square root of the number of lines used), atmospheric parameter uncertainties ($\sigma_{T_{\text{eff}}}$, σ_{logg} , σ_{ξ_t}), and the Fe abundance error (σ_{Fe})

$$\sigma_{\text{tot}} = \sqrt{\left(\frac{\sigma_{121}}{\sqrt{N_{\text{ion}}}}\right)^2 + (\sigma_{T_{\text{eff}}})^2 + (\sigma_{\text{logg}})^2 + (\sigma_{\xi_t})^2 + \left(\frac{\sigma_{\text{Fe}}}{\sqrt{N_{\text{Fe}}}}\right)^2}.$$

Table 4. Abundance results of IRAS 06530-0213, IRAS 22223+4327, and both observations of IRAS08143-4406. The list of IRAS08143 BLUE437 contains the results for the Blue437 and Red860 spectra, the list of IRAS08143 RED580 shows the results for the Red580 spectra (see Sect. 2).

Ion	log ϵ_{\odot}	IRAS06530 [Fe/H] = -0.32 $T_{\text{eff}} = 7375\text{K}$ log $g = 1.25$ dex					IRAS08143 BLUE437 [Fe/H] = -0.43 $T_{\text{eff}} = 7000\text{K}$ log $g = 1.5$ dex					IRAS08143 RED580 [Fe/H] = -0.36 $T_{\text{eff}} = 7250\text{K}$ log $g = 1.50$ dex					IRAS22223 [Fe/H] = -0.30 $T_{\text{eff}} = 6500\text{K}$ log $g = 1.00$ dex				
		N	log ϵ	σ_{121}	[X/Fe]	σ_{tot}	N	log ϵ	σ_{121}	[X/Fe]	σ_{tot}	N	log ϵ	σ_{121}	[X/Fe]	σ_{tot}	N	log ϵ	σ_{121}	[X/Fe]	σ_{tot}
C I	8.43	10	8.94	0.07	0.83	0.13	15	8.71	0.06	0.71	0.10	11	8.74	0.09	0.67	0.12	19	8.72	0.06	0.59	0.07
N I	7.83						7	7.41	0.30	0.01	0.22						2	7.68	0.30	0.15	0.21
O I	8.69	6	8.72	0.08	0.35	0.11						3	8.52	0.04	0.19	0.13	5	8.70	0.06	0.31	0.13
Na I	6.24	1	6.32	0.20	0.46	0.22						2	6.35	0.08	0.48	0.11	2	6.20	0.04	0.28	0.08
Mg I	7.60	1	7.22	0.20	-0.0	0.23	4	7.21	0.06	0.05	0.09	2	7.22	0.04	-0.01	0.10	1	7.30	0.20	0.02	0.22
Al I	6.45						2	6.40	0.01	0.40	0.09	1	6.42	0.20	0.34	0.22	2	6.10	0.04	-0.03	0.09
Si I	7.51	2	7.34	0.13	0.15	0.22	4	7.54	0.06	0.46	0.17	7	7.66	0.08	0.51	0.18	14	7.42	0.10	0.21	0.17
Si II	7.51	1	7.36	0.20	0.17	0.24															
P I	5.41						1	5.80	0.20	0.82	0.26										
S I	7.12	3	7.00	0.05	0.21	0.18	7	7.10	0.08	0.41	0.14	3	7.10	0.01	0.34	0.15	5	6.94	0.08	0.12	0.12
Ca I	6.34	12	6.18	0.09	0.22	0.09	3	6.15	0.07	0.26	0.09	12	6.16	0.09	0.18	0.08	8	6.01	0.08	-0.01	0.07
Ca II	6.34	2	6.08	0.01	0.06	0.10						4	6.11	0.07	0.13	0.10	3	6.00	0.07	-0.04	0.10
Sc II	3.15	5	3.15	0.03	0.33	0.09						2	3.09	0.04	0.30	0.10	4	2.95	0.10	0.10	0.11
Ti I	4.95						5	5.03	0.13	0.53	0.11	5	5.06	0.07	0.47	0.09					
Ti II	4.95	5	4.79	0.05	0.16	0.09						5	5.01	0.09	0.42	0.10	5	4.54	0.12	-0.11	0.11
V II	3.93						2	3.75	0.01	0.25	0.12	1	3.74	0.20	0.17	0.24	4	3.64	0.17	0.01	0.15
Cr I	5.64	2	5.45	0.03	0.19	0.09	4	5.33	0.07	0.13	0.09	4	5.41	0.11	0.13	0.11	6	5.22	0.11	-0.1	0.09
Cr II	5.64	11	5.36	0.07	0.04	0.07	2	5.31	0.06	0.10	0.11	13	5.31	0.06	0.03	0.07	11	5.29	0.06	-0.05	0.06
Mn I	5.43	2	4.99	0.20	-0.07	0.19	3	5.05	0.03	0.07	0.08	2	5.05	0.20	-0.02	0.19	2	4.98	0.03	-0.13	0.08
Mn II	5.43						1	5.08	0.20	0.08	0.23	1	5.05	0.20	-0.01	0.23					
Fe I	7.50	54	7.12	0.08	0.00	0.05	17	7.05	0.08	0.00	0.06	70	7.13	0.08	0.00	0.04	80	7.18	0.06	0.00	0.04
Fe II	7.50	24	7.18	0.08	0.00	0.06	8	7.07	0.10	0.00	0.10	23	7.14	0.09	0.00	0.06	25	7.20	0.07	0.00	0.05
Co II	4.99																1	4.71	0.20	0.02	0.23
Ni I	6.22	5	6.07	0.05	0.23	0.08	13	6.06	0.08	0.28	0.07	4	6.08	0.05	0.22	0.08	13	5.87	0.07	-0.03	0.06
Ni II	6.22	1	6.15	0.20	0.25	0.23															
Cu I	4.19	1	4.39	0.20	0.58	0.22						1	4.32	0.20	0.50	0.22	1	4.09	0.20	0.22	0.22
Zn I	4.56	1	4.70	0.20	0.46	0.30						1	4.60	0.20	0.40	0.29	3	4.36	0.09	0.10	0.19
Y II	2.21	2	3.79	0.11	1.91	0.16	3	3.63	0.04	1.85	0.11	2	3.65	0.02	1.80	0.12	3	3.24	0.08	1.33	0.11
Zr II	2.58	2	3.86	0.04	1.60	0.10	5	3.85	0.13	1.70	0.12	4	3.85	0.10	1.63	0.11	3	3.63	0.06	1.35	0.10
Mo II	1.88																1	2.89	0.20	1.31	0.23
Ba II	2.18						1	3.45	0.20	1.70	0.27						1	2.89	0.20	1.01	0.26
La II	1.10	7	3.06	0.05	2.28	0.16	18	2.47	0.05	1.80	0.11	14	2.46	0.10	1.72	0.14	14	1.87	0.11	1.07	0.12
Ce II	1.58	10	3.31	0.12	2.05	0.15	7	2.61	0.04	1.46	0.11	5	2.56	0.10	1.35	0.14	5	2.30	0.10	1.02	0.13
Pr II	0.72	5	2.75	0.07	2.35	0.19	6	2.15	0.07	1.85	0.16	9	2.10	0.09	1.74	0.17	5	1.44	0.07	1.02	0.15
Nd II	1.42	16	3.31	0.07	2.21	0.18	12	2.70	0.06	1.71	0.14	19	2.67	0.09	1.61	0.16	13	1.96	0.11	0.85	0.15
Sm II	0.96	2	2.25	0.04	1.61	0.17	16	1.90	0.04	1.37	0.12	6	1.91	0.08	1.31	0.15	8	1.25	0.10	0.59	0.14
Eu II	0.52	2	1.56	0.01	1.36	0.17						2	1.10	0.01	0.94	0.14	2	0.78	0.14	0.56	0.16
Gd II	1.07	5	2.59	0.11	1.84	0.13	8	2.00	0.06	1.36	0.09	2	2.02	0.01	1.31	0.11	1	1.67	0.20	0.90	0.23
Dy II	1.10																1	1.80	0.20	1.00	0.24
Er II	0.92	2	2.88	0.07	2.29	0.15	2	2.20	0.20	1.71	0.20	1	2.20	0.20	1.64	0.24	1	1.18	0.20	0.56	0.23
Tm II	0.10	1	1.45	0.20	1.67	0.24															
Yb II	0.84	1	2.72	0.20	2.21	0.25	1	2.15	0.20	1.74	0.25	1	2.12	0.20	1.64	0.25					
Lu II	0.10	3	1.85	0.20	2.07	0.19						1	1.00	0.20	1.26	0.25					
Hf II	0.85	1	2.43	0.20	1.91	0.22															
W II	0.85	1	2.98	0.20	2.45	0.25						1	2.15	0.20	1.66	0.25	1	1.45	0.20	0.90	0.25

Notes: Same as for Table 3.

- (1) ion. In other words, if the ionisation potential of an ion is below the ionisation potential of Fe I, the Fe I abundance is used for calculating [X/Fe]. If the ionisation potential exceeds the ionisation potential of Fe I, the abundance of Fe II is used instead.

We assume an intrinsic uncertainty of 0.2 dex for all elemental abundances, which are determined by only one line or via spectrum synthesis. This error is a substitute of the line-to-line scatter determined for elements with more useful lines. The [X/Fe] abundances are calculated using the Fe ion with an ionisation potential closest to the ionisation potential of the studied

In Tables 3 to 6, all elemental abundances were double-checked by comparing each spectral line with synthetic spectra with the determined abundances. Examples of these com-

Table 5. Abundance results of IRAS 07134+1005, IRAS 08281-4850, IRAS 17279-1119, and IRAS 19500-1709.

Ion	$\log \epsilon_{\odot}$	IRAS07134 [Fe/H] = -0.91 $T_{\text{eff}} = 7250$ K $\log g = 0.5$ dex					IRAS08281 [Fe/H] = -0.26 $T_{\text{eff}} = 7875$ K $\log g = 1.25$ dex					IRAS17279 [Fe/H] = -0.64 $T_{\text{eff}} = 7250$ K $\log g = 1.25$ dex					IRAS19500 [Fe/H] = -0.59 $T_{\text{eff}} = 8000$ K $\log g = 1.00$ dex				
		N	$\log \epsilon$	σ_{121}	[X/Fe]	σ_{tot}	N	$\log \epsilon$	σ_{121}	[X/Fe]	σ_{tot}	N	$\log \epsilon$	σ_{121}	[X/Fe]	σ_{tot}	N	$\log \epsilon$	σ_{121}	[X/Fe]	σ_{tot}
C I	8.43	47	8.68	0.08	1.16	0.22	16	8.91	0.05	0.75	0.21	17	8.36	0.09	0.47	0.14	15	8.82	0.06	0.99	0.33
N I	7.83	3	7.50	0.30	0.57	0.19						1	7.27	0.30	-0.07	0.35	3	7.65	0.30	0.41	0.17
O I	8.69	9	8.59	0.06	0.81	0.19	5	8.54	0.06	0.12	0.11	2	8.39	0.05	0.24	0.16	8	8.81	0.04	0.72	0.09
Na I	6.24						1	6.65	0.20	0.70	0.22	2	6.25	0.05	0.52	0.11					
Mg I	7.60	4	6.89	0.06	0.26	0.13	3	7.38	0.09	0.07	0.10	2	7.25	0.06	0.16	0.12	2	7.31	0.01	0.29	0.07
Mg II	7.60																3	7.29	0.00	0.28	0.10
Al I	6.45																1	5.51	0.20	-0.36	0.21
Si I	7.51						2	7.50	0.20	0.25	0.31	6	7.33	0.10	0.36	0.20	1	7.03	0.20	0.11	0.49
Si II	7.51											1	7.33	0.20	0.36	0.26	2	7.01	0.06	0.10	0.13
S I	7.12	1	6.59	0.20	0.38	0.35	3	7.24	0.03	0.38	0.24	2	6.91	0.02	0.33	0.18					
K I	5.03	2	4.68	0.07	0.61	0.12											3	6.08	0.06	0.32	0.23
Ca I	6.34	11	5.44	0.05	0.07	0.11	5	6.29	0.08	0.25	0.15	7	6.00	0.07	0.17	0.09	3	5.92	0.08	0.18	0.26
Ca II	6.34	3	5.47	0.03	0.04	0.18	2	6.18	0.03	0.10	0.16	1	6.00	0.20	0.20	0.25	3	5.92	0.08	0.18	0.26
Sc II	3.15	8	2.41	0.06	0.17	0.09	5	3.19	0.04	0.30	0.13	7	2.71	0.09	0.10	0.12	8	2.78	0.11	0.23	0.22
Ti I	4.95											3	4.62	0.06	0.18	0.12					
Ti II	4.95	24	4.18	0.09	0.14	0.08	12	4.74	0.04	0.05	0.09	16	4.65	0.13	0.24	0.10	33	4.54	0.09	0.19	0.14
V II	3.93	5	3.32	0.10	0.30	0.11	1	3.68	0.20	0.02	0.24	5	3.92	0.10	0.53	0.13	11	3.62	0.10	0.28	0.12
Cr I	5.64	3	4.70	0.14	0.03	0.16	1	5.40	0.20	0.05	0.22	2	5.17	0.03	0.04	0.11	3	5.12	0.10	0.06	0.11
Cr II	5.64	14	4.85	0.09	0.12	0.10	12	5.33	0.05	-0.05	0.06	13	5.14	0.11	0.04	0.10	24	5.14	0.10	0.10	0.07
Mn I	5.43	2	4.56	0.04	0.10	0.09											2	4.75	0.03	-0.09	0.09
Mn II	5.43	4	4.52	0.08	0.00	0.16						2	5.03	0.10	0.13	0.15	5	4.91	0.04	0.07	0.06
Fe I	7.50	42	6.53	0.07	0.00	0.05	44	7.21	0.07	0.00	0.04	44	6.99	0.10	0.00	0.06	33	6.92	0.06	0.00	0.04
Fe II	7.50	32	6.59	0.09	0.00	0.06	23	7.24	0.07	0.00	0.05	30	6.96	0.13	0.00	0.08	32	6.91	0.03	0.00	0.03
Co I	4.99											2	4.28	0.14	-0.2	0.17					
Co II	4.99																1	4.70	0.20	0.31	0.22
Ni I	6.22	5	5.34	0.08	0.09	0.09						4	6.13	0.11	0.43	0.12	3	5.79	0.08	0.15	0.08
Ni II	6.22	1	5.32	0.20	0.01	0.26	2	5.90	0.20	-0.06	0.19	4	6.07	0.07	0.39	0.11	2	5.80	0.07	0.18	0.09
Zn I	4.56											1	4.25	0.20	0.23	0.31					
Y II	2.21	12	2.97	0.12	1.67	0.13	7	3.66	0.06	1.72	0.19	10	2.38	0.12	0.71	0.12	11	3.02	0.11	1.40	0.29
Zr II	2.58	15	3.28	0.09	1.61	0.09	12	3.74	0.10	1.42	0.11	10	2.82	0.11	0.77	0.12	22	3.32	0.10	1.34	0.19
Mo II	1.88	1	2.68	0.20	1.71	0.27	1	3.35	0.20	1.73	0.23						2	2.88	0.08	1.60	0.12
Ba II	2.18	2	3.09	0.02	1.82	0.30	1	3.80	0.20	1.88	0.36	1	2.80	0.20	1.16	0.31	1	3.00	0.20	1.42	0.49
La II	1.10	29	2.04	0.09	1.85	0.24	17	2.70	0.11	1.87	0.28	7	1.48	0.13	0.92	0.17	5	1.87	0.09	1.37	0.43
Ce II	1.58	41	2.27	0.11	1.59	0.20	21	2.85	0.08	1.54	0.24	11	2.02	0.10	0.98	0.15	7	2.28	0.12	1.29	0.39
Pr II	0.72	5	1.43	0.08	1.62	0.31	3	2.40	0.20	1.94	0.34	5	1.35	0.11	1.17	0.21					
Nd II	1.42	29	2.14	0.08	1.63	0.29	15	2.83	0.09	1.67	0.30	8	1.64	0.07	0.75	0.19	5	2.31	0.03	1.48	0.44
Sm II	0.96	13	1.49	0.07	1.44	0.26						3	1.46	0.08	1.03	0.19					
Eu II	0.52	2	0.20	0.20	0.59	0.32	2	1.00	0.20	0.74	0.33						1	1.10	0.20	1.18	0.48
Gd II	1.07	6	1.33	0.08	1.17	0.19	2	1.98	0.02	1.18	0.18						2	1.52	0.18	1.05	0.34
Dy II	1.10	2	1.14	0.20	0.95	0.28	1	1.90	0.20	1.06	0.33										
Er II	0.92	2	1.41	0.00	1.40	0.22	1	2.19	0.20	1.54	0.30										
Lu II	0.10	4	0.80	0.20	1.61	0.22	1	1.30	0.20	1.46	0.25	1	0.50	0.20	0.94	0.27	2	0.64	0.10	1.13	0.21
Hf II	0.85						2	2.35	0.20	1.76	0.20	1	1.04	0.20	0.72	0.25	1	1.53	0.20	1.27	0.25

Notes: Same as for Table 3.

parisons are shown in Figs. 5, 6, and 7. Fig. 5 shows a spectrum synthesis check for the determined C abundance of IRAS 22223+4327. The red synthetic spectrum computed using the determined elemental abundances fits the observed spectrum well, except for the strong spectral line at 6006 Å. To investigate its identification, we artificially increased the abundances of all elements with spectral lines in this spectral region, but none could produce the observed absorption. This shows that the linelists are not complete for our strongly *s*-process enriched stars, the spectra of which are swamped with transitions of *s*-

process elements. Also, for other stars and different spectral regions, we find spectral lines not included in the linelists.

Fig. 6 shows a spectrum synthesis check of the determined Nd abundance of IRAS 06530-0213 for the Nd II lines at 6031.270 and 6034.228 Å, confirming the high Nd abundance of IRAS 06530-0213. The spectrum synthesis of the high excitation O I triplet at 6156 Å of IRAS 13245-5036 is shown in Fig. 7 and shows a good agreement between the observations and determined O abundances.

We briefly discuss the derived abundances followed by the comparison between our determined results and those of previ-

Table 6. Abundance results of IRAS 13245-5036, IRAS 14325-6428, and IRAS 14429-4539.

Ion	$\log \epsilon_{\odot}$	IRAS13245 [Fe/H] = -0.30 $T_{\text{eff}} = 9500$ K $\log g = 2.75$ dex					IRAS14325 [Fe/H] = -0.56 $T_{\text{eff}} = 8000$ K $\log g = 1.00$ dex					IRAS14429 [Fe/H] = -0.18 $T_{\text{eff}} = 9375$ K $\log g = 2.50$ dex				
		N	$\log \epsilon$	σ_{121}	[X/Fe]	σ_{tot}	N	$\log \epsilon$	σ_{121}	[X/Fe]	σ_{tot}	N	$\log \epsilon$	σ_{121}	[X/Fe]	σ_{tot}
C I	8.43	4	8.70	0.00	0.57	0.21	24	9.06	0.10	1.18	0.23	3	8.93	0.08	0.68	0.23
N I	7.83						7	7.45	0.30	0.18	0.20					
O I	8.69	5	8.65	0.12	0.26	0.13	10	8.70	0.06	0.57	0.09	6	8.82	0.04	0.31	0.12
Na I	6.24						1	6.50	0.20	0.81	0.22					
Mg I	7.60	5	7.16	0.07	-0.09	0.09	4	7.51	0.05	0.47	0.08	3	7.32	0.04	-0.01	0.09
Mg II	7.60	2	7.20	0.07	-0.11	0.11	5	7.37	0.13	0.33	0.14	3	7.29	0.03	-0.13	0.10
Al I	6.45	1	5.75	0.20	-0.35	0.23	1	5.70	0.20	-0.2	0.21	2	5.89	0.01	-0.3	0.09
Al II	6.45											1	5.97	0.20	-0.3	0.26
Si I	7.51	1	7.19	0.20	-0.02	0.33	1	6.85	0.20	-0.1	0.38	1	7.10	0.20	-0.23	0.33
Si II	7.51	3	7.19	0.07	-0.02	0.12	2	6.83	0.00	-0.12	0.18	1	7.15	0.20	-0.18	0.25
S I	7.12						1	7.20	0.20	0.64	0.32					
Ca I	6.34						5	6.23	0.10	0.44	0.21					
Ca II	6.34						2	6.26	0.03	0.48	0.20					
Sc II	3.15	6	3.29	0.11	0.44	0.18	11	2.97	0.11	0.38	0.19	8	3.38	0.12	0.41	0.20
Ti II	4.95	22	4.96	0.10	0.31	0.12	28	4.57	0.07	0.18	0.12	42	5.03	0.10	0.26	0.12
V II	3.93	2	3.73	0.03	0.10	0.11	11	3.60	0.09	0.23	0.12	4	3.99	0.09	0.24	0.13
Cr I	5.64						3	5.28	0.09	0.19	0.10					
Cr II	5.64	11	5.44	0.07	0.10	0.07	22	5.19	0.07	0.11	0.05	28	5.51	0.09	0.05	0.07
Mn I	5.43						1	4.94	0.20	0.06	0.23					
Mn II	5.43											2	5.30	0.04	0.05	0.10
Fe I	7.50	21	7.15	0.10	0.00	0.07	26	6.95	0.06	0.00	0.04	26	7.24	0.09	0.00	0.06
Fe II	7.50	41	7.20	0.06	0.00	0.04	58	6.94	0.06	0.00	0.04	52	7.32	0.09	0.00	0.05
Ni I	6.22						3	5.78	0.06	0.12	0.08					
Ni II	6.22	4	5.93	0.07	0.01	0.09	4	5.74	0.10	0.08	0.10	4	5.97	0.10	-0.07	0.11
Y II	2.21	11	3.31	0.04	1.40	0.23	10	2.99	0.12	1.34	0.26	10	3.15	0.10	1.13	0.25
Zr II	2.58	17	4.00	0.08	1.72	0.15	17	3.18	0.12	1.16	0.16	13	3.86	0.10	1.46	0.17
Ba II	2.18	1	4.00	0.20	2.12	0.34	1	3.10	0.20	1.48	0.42					
La II	1.10	3	3.02	0.10	2.22	0.28	7	1.85	0.06	1.31	0.35	4	2.61	0.11	1.69	0.29
Ce II	1.58	4	3.40	0.20	2.12	0.28	3	2.29	0.20	1.27	0.35					
Pr III	0.72	2	2.83	0.08	2.41	0.11										
Nd II	1.42						2	2.25	0.20	1.39	0.40					
Nd III	1.42	12	3.30	0.07	2.18	0.07						15	2.94	0.09	1.70	0.08
Sm II	0.96						1	1.75	0.20	1.35	0.41					
Eu II	0.52						1	0.75	0.20	0.79	0.41					
Gd II	1.07						1	1.76	0.20	1.25	0.34					
Dy II	1.10						1	1.48	0.20	0.94	0.39					
Dy III	1.10	1	2.79	0.20	1.99	0.23										
Lu II	0.10						1	0.85	0.20	1.31	0.28					
Hf II	0.85						1	1.53	0.20	1.24	0.25	1	2.54	0.20	1.87	0.25

Notes: Same as for Table 3.

ous studies. In Sect. 5, we specifically discuss the derived Pb abundances.

4.1. CNO elements

For all programme stars, we can determine the carbon and oxygen abundances. The C/O ratios range from about 1.0 up to 2.5 and are listed in the second column of Table 8. The errors on the C/O ratios in Table 8 include line-to-line scatter and atmospheric model uncertainties. They can become significant because of the strong temperature sensitivity of the available C and O lines within the temperature range of the sample stars. The two new post-AGB stars, IRAS 13245-5036 and IRAS 14429-4539, display C/O ratios of about 1.1 and 1.3, respectively. This also

confirms the observation that the 21 μm feature is only detected around carbon-rich post-AGB stars.

For six of the stars, we could determine nitrogen abundances using non-LTE sensitive spectral lines between 7000 and 9000 \AA . We applied non-LTE corrections to the LTE N abundances following the temperature-dependent corrections of Fig. 4 in Lyubimkov et al. (2011), which shows a larger correction for higher temperatures. We adopted the following corrections: for IRAS 22223+4327, we use a correction of -0.3 dex; for IRAS 08143-4406, we apply a correction of -0.4 dex; for IRAS 07143+1005 and IRAS 17279-1119, we apply corrections of -0.5 dex; and for IRAS 14325-6428 and IRAS 19500-1709, we use corrections of -0.65 dex and -0.7 dex, respectively. These corrections are already included in the listed results of Tables 4,

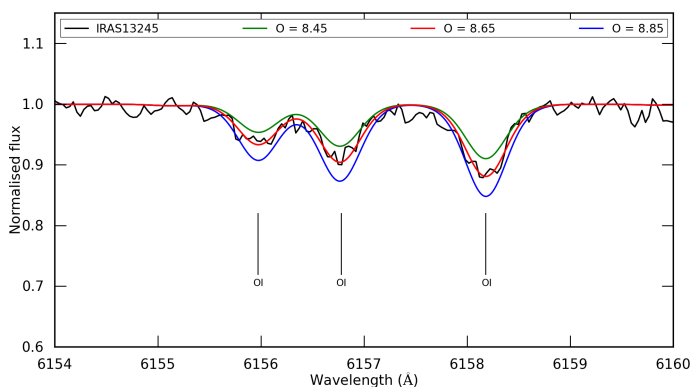


Fig. 7. Spectrum synthesis of the O I triplet at 6156 Å for IRAS 13245-5036. The black spectrum is the observed UVES spectrum, the coloured spectra represent synthetic spectra with different O abundances. The red line represents the determined O abundance; the green and blue spectra represent synthetic spectra with an O abundance of -0.2 dex and +0.2 dex, respectively.

5, and 6. Given the uncertainties on the non-LTE correction, we assume a somewhat ad-hoc, line-to-line scatter of 0.3 dex for all N abundance determinations.

4.2. *S*-process elements

The two new post-AGB stars, IRAS 13245-5036 and IRAS 14429-4539, show strong *s*-process enrichments with a stronger overabundance of the *h*s elements with respect to the *l*s elements. Both stars are warm and, hence, intrinsically display a less rich spectrum. We could only determine a limited set of *s*-process elements for IRAS 14429-4539. The *s*-process enrichments confirm the evolved nature of both stars. This corroborates the finding that the stars displaying the 21 μm feature are all *s*-process rich and carbon-rich post-AGB stars, which are the likely descendants of AGB carbon stars.

We confirm that all other programme stars show *s*-process enhancements for both the *l*s and *h*s elements with significant differences between the objects. IRAS 17279-1119 displays a mild *s*-process enrichment and most of the *s*-process elements have an $[X/Fe] < 1.0$ dex, while the two strongest enriched objects, IRAS 05341+0852 and IRAS 06530-0213, have high *s*-process $[X/Fe]$ abundances reaching up to 2.5 dex. The abundances derived from the two observational settings are similar for IRAS 08143-4406 (upper right panel of Fig. 9).

Apart from the different levels of enrichment, we also find different abundance distributions. For IRAS 08143-4406, IRAS 14325-6428, IRAS 19500-1709, and IRAS 22223+4327, the enrichment of the *l*s elements Y and Zr is higher or similar to that of the *h*s elements, while for the other stars the situation is reversed. We go into more detail about the *h*s/*l*s behaviour in Sect. 6.

For those objects with Mo determination, we find that Mo has similar enhancements as Y and Zr. The elements with $Z > 62$ are also enriched and their abundance distributions strongly vary from star to star to a level comparable to or less than that of the *h*s elements.

4.3. Comparison with previous studies

As online material in Appendix B, we provide the comparison between our abundance results and those of previous abundance studies (see second to last column of Table 1). For IRAS 13245-

5036 and IRAS 14429-4539, there are no available data in literature. We remark that previous studies used different linelists and solar abundances, which can explain small differences between our determinations and previous determinations. Especially, changes in oscillator strength $\log gf$ can significantly impact the individual spectral line abundances.

5. Pb abundance determination

For each star, we use an artificially high abundance to theoretically predict which optical Pb line (Pb I or Pb II) is the strongest for a specific set of atmospheric parameters. We then select the Pb line that gives the largest predicted EW. For some stars, both Pb lines result in a similar theoretical EW, so we can use both lines to constrain the Pb abundance.

Depending on the effective temperature of the sample stars, the Pb abundances are probed either using the strongest Pb I line at 4057.807 Å or Pb II line at 5608.853 Å. As the Pb I line lies in a low S/N region with many spectral blends and the Pb II line is generally very small so that it can be confused with noise in the spectrum, none of the sample stars display a clear Pb line feature from which an accurate Pb abundance can be derived. Therefore, we can only determine upper limits on the Pb abundance.

We generate synthetic spectra for the spectral region of the Pb line, including all the derived abundances; these are listed in Tables 3 to 6. We use the synthetic spectral lines to estimate the local position of the continuum at the Pb line. The lowest Pb abundance for which the synthetic spectrum fully includes the observed spectral blend at the Pb line is adopted as upper limit of the Pb abundance. Examples of our method are illustrated in Figs. 11, 12, and 13 for three different sample stars.

Fig. 11 shows the Pb abundance determination of IRAS 22223+4327 using the Pb I line at 4057.807 Å. For stars with lower temperatures and/or high metallicities, this spectral region contains many spectral blends. The S/N in this blue region is generally only between 20 and 30. We use the identified spectral blends at 4057.5 Å and 4058.9 Å to estimate the position of the continuum and then use different synthetic Pb abundances to determine the upper limit. For each figure, the red synthetic spectra represent our adopted abundance upper limit and the dashed black lines show synthetic spectra without any Pb contribution included.

In case of IRAS 22223+4327, there is no clear contribution from Pb. The blue synthetic spectrum in Fig. 11 provides a full observed feature around 4057.807 Å, but generates a large contribution to the blend with the line at 4057.5 Å that is not observed in the spectrum. Therefore, we adopt an upper limit of the Pb abundance for IRAS 22223+4327, which only creates a contribution to the blend that is still compliant with the observed spectrum. Fig. 11 also shows that there are a number of spectral lines in this region that are not included in the linelists. The line features at 4056.2 Å and 4060.5 Å are examples. Moreover, for stars with $T_{\text{eff}} < 7500$ K and $[Fe/H] > 0.5$ dex, we cannot reproduce the blended line at 4058.2 Å at the red side of the Pb I line, which would otherwise be a major factor for constraining the local continuum position.

The Pb abundance determinations of IRAS 06530-0213 are presented in Fig. 12. The upper panel shows the determination via the Pb I line at 4057.807 Å; the lower panel shows the same for the Pb II line at 5608.853 Å. Also, for this star, we do not detect a clear Pb I line and we use the spectral blends at 4057.5 and 4058.9 Å to estimate the position of the continuum. We adopt a Pb abundance that generates a synthetic Pb line, which fully

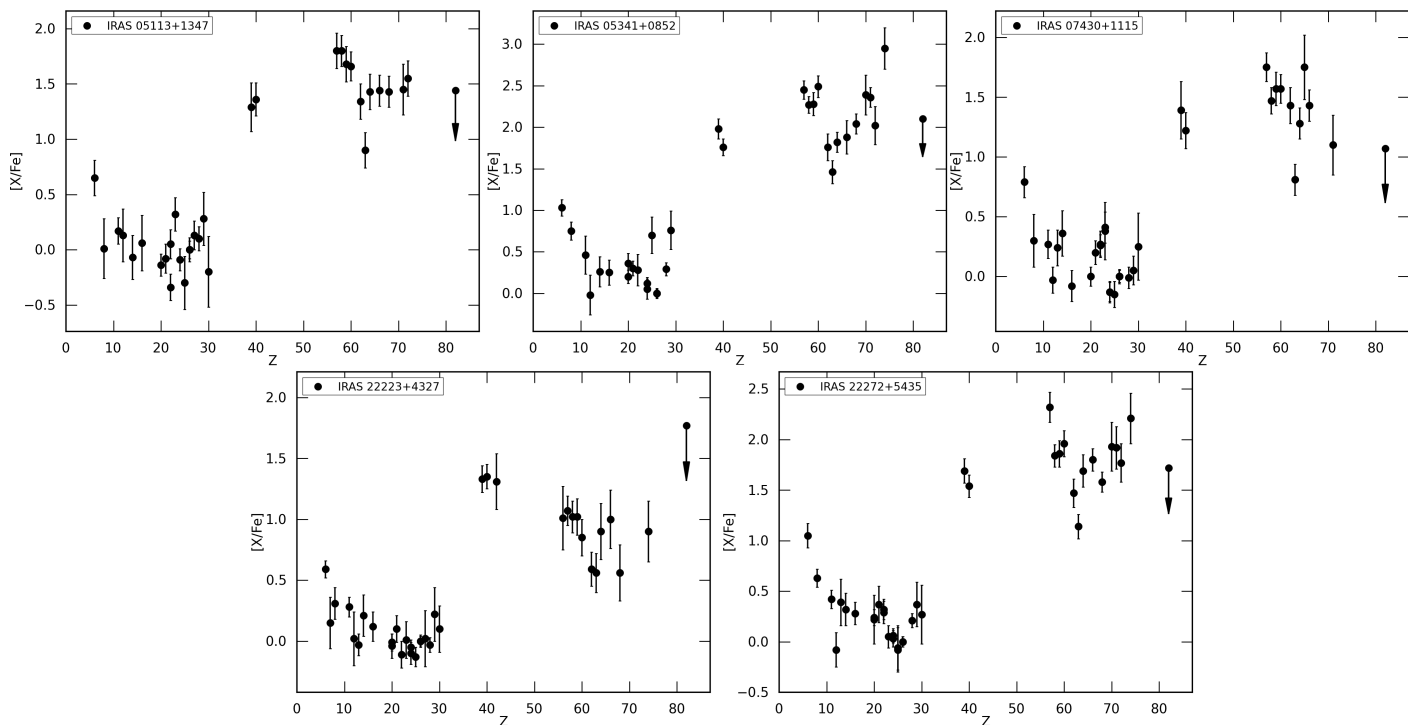


Fig. 8. Element-over-iron ratios for the programme stars with $T_{\text{eff}} < 7000$ K. The down arrow at $Z=82$ displays the adopted Pb abundance upper limits.

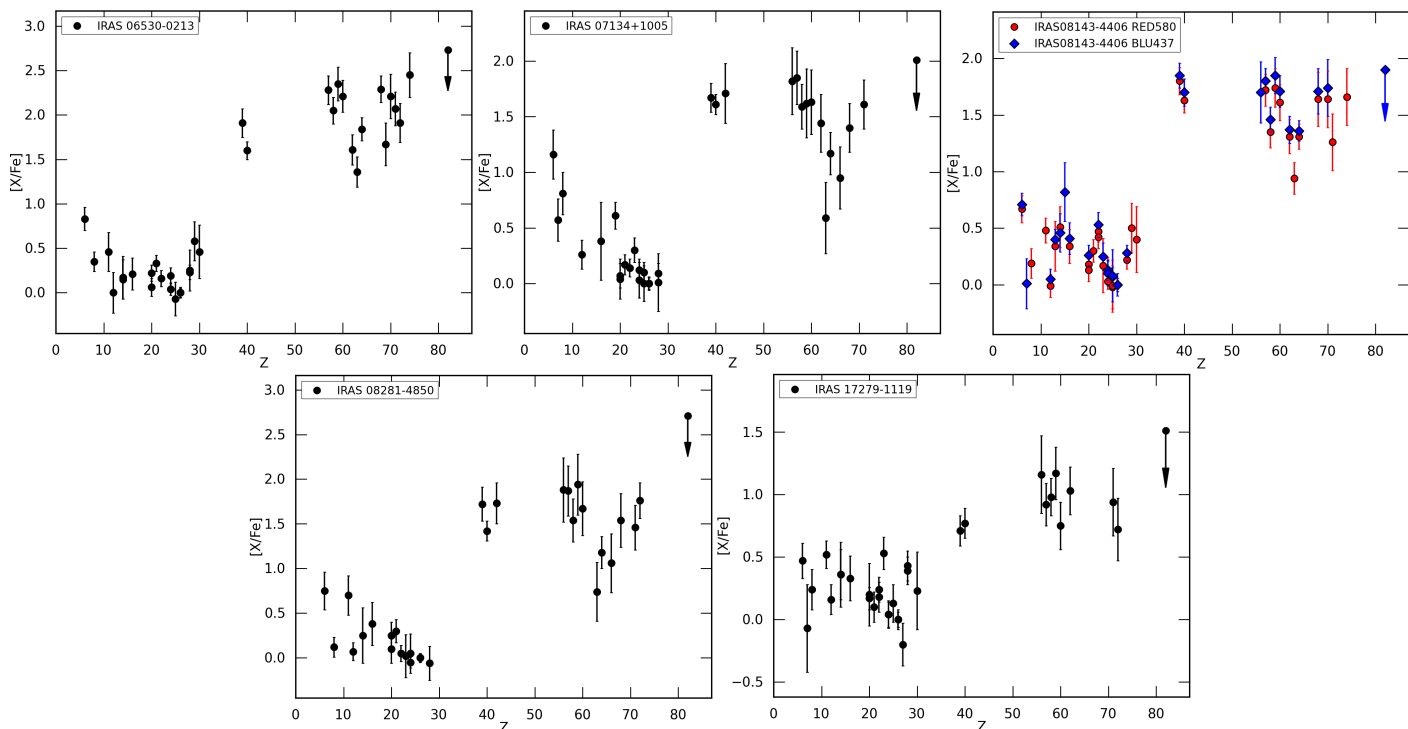


Fig. 9. Element-over-iron ratios for the programme stars with $7000 \text{ K} \leq T_{\text{eff}} < 8000$ K. The down arrow at $Z=82$ displays the adopted Pb abundance upper limits. For IRAS 08143-4406, the abundance results of both observational settings are shown.

incorporates the observed line feature at 4057.807 \AA . For the Pb II line at 5608.853 \AA , we use the continuum between 5606.3 and 5608 \AA in combination with the blend at 5610.3 \AA to estimate the position of the continuum at 5608.853 \AA . The Pb II line lies in a spectral region where the continuum is affected by a blend of small unidentified spectral lines, ranging from 5608 up to 5610 \AA . The observed spectrum lies below the continuum of the

synthetic spectra. To make sure this feature is real, we checked the individual observed spectra of IRAS 06530-0213 in Table 1 and found the feature to be present in both observations. We also compared our new spectra with the old observations from Reyniers et al. (2004) and this broad feature is present there as well. We therefore expect this depression to be real. This is likely a set of unresolved small lines. For the Pb II line, we adopt a Pb

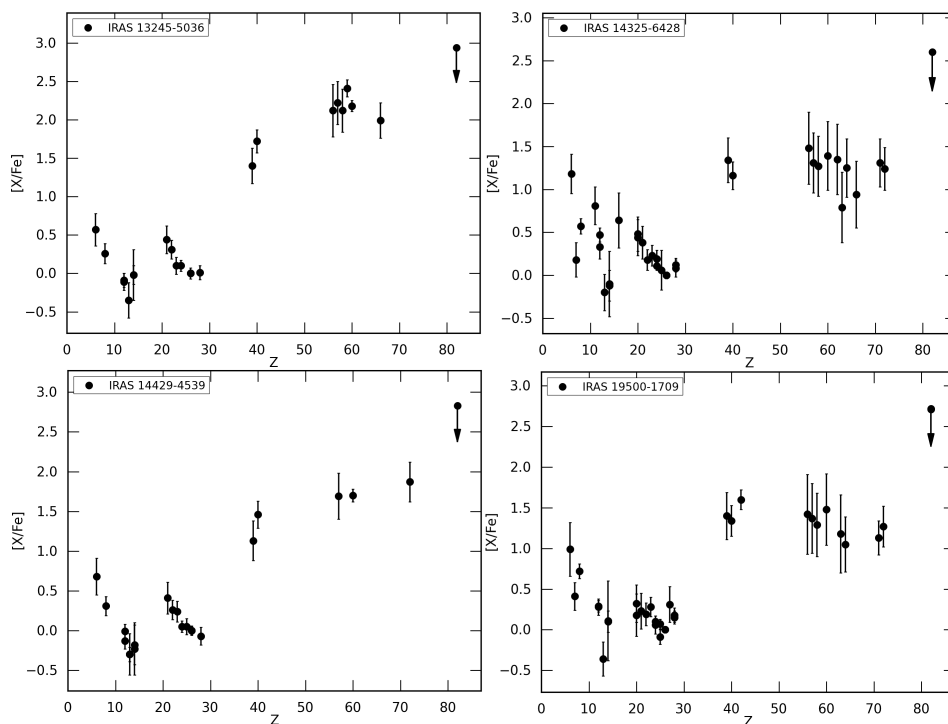


Fig. 10. Element-over-iron ratios for the programme stars with $T_{\text{eff}} \geq 8000$ K. The down arrow at $Z=82$ displays the adopted Pb abundance upper limits.

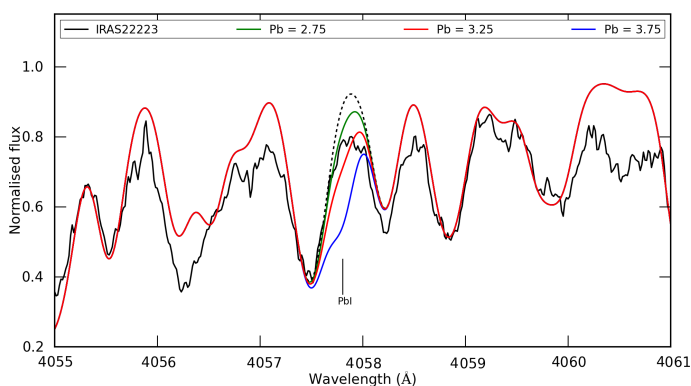


Fig. 11. Spectrum synthesis of the Pb I line at 4057.807 \AA for IRAS 22223+4327. The black spectrum is the observed HERMES spectrum, the coloured spectra represent synthetic spectra with different Pb abundances. The red line represents the adopted Pb abundance upper limit; the green and blue lines represent the adopted abundance upper limit -0.5 dex and $+0.5$ dex, respectively. The dashed black line shows the synthetic spectrum if no Pb is present. For more information, see text.

abundance that fits the observed spectrum. However, comparison with the spectra of Reyniers et al. (2004) suggest that the small line at 5608.853 \AA in the broad feature between 5608 and 5610 \AA is not significant as it is not seen in the older spectra. As a result of this possibility, in combination with the lower upper limit found for the Pb I line, we adopt the limit for the Pb I line as the upper limit of the Pb abundance for IRAS 06530-0213.

Fig. 13 shows the Pb abundance determination for IRAS 13245-5036 with the Pb II line at 5608.853 \AA . We do not detect any Pb II line feature for this star, and therefore we adopt an upper limit of the Pb abundance, which creates a synthetic Pb II line that lies slightly below the observed spectrum. The Pb I line at 4057.807 \AA would need a significantly higher Pb abundance

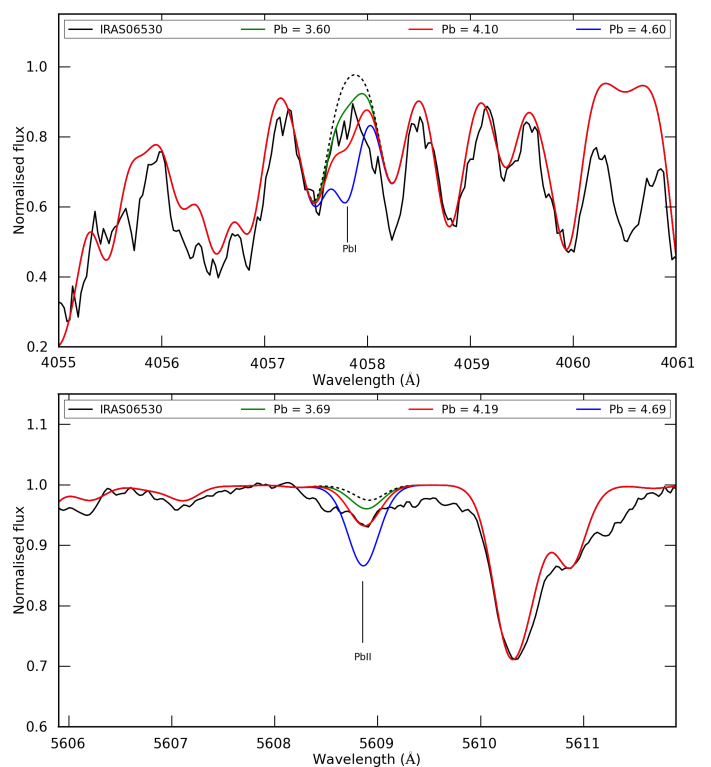


Fig. 12. Spectrum synthesis of the Pb I line at 4057.807 \AA (upper panel) and of the Pb II line at 5608.853 \AA (lower panel) for the UVES spectra of IRAS 06530-0213. Lines and symbols are similar to Fig. 11.

than the adopted upper limit based on the Pb II line. Therefore, we only consider the upper limit based on the Pb II line.

The determinations of the upper limits on the Pb abundances of all other programme stars are presented and discussed in Appendix A, which is provided as online material for this paper. We

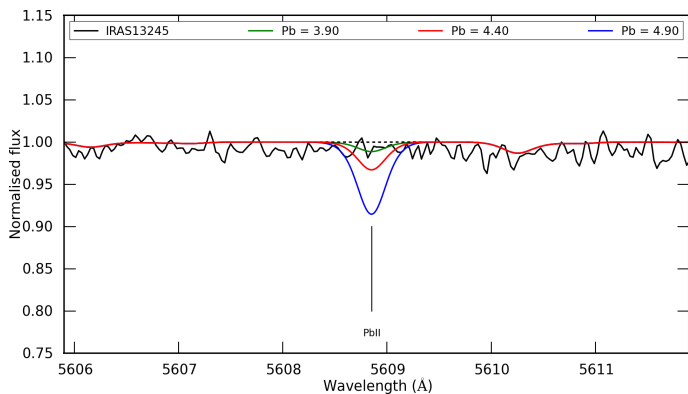


Fig. 13. Spectrum synthesis of the Pb II line at 5608.853 Å for the UVES spectrum of IRAS 13245-5036. Lines and symbols are similar to Figs. 11 and 12.

do not detect strong Pb lines for any of the 14 *s*-process enriched post-AGB stars. For the remaining part of the paper, we therefore refer to the Pb upper limit abundances as Pb_{up} . In Table 7, we list the individual Pb upper limit abundance results for the Pb I and Pb II line of the programme stars. The element-over-iron ratios corresponding to the adopted Pb abundance are shown in Figs. 8, 9, and 10, and indicated with down arrows. The last six rows display the results of De Smedt et al. (2014, 2015) for six carbon and *s*-process enhanced post-AGB stars in the Magellanic Clouds and are used in the analysis of the neutron irradiation in Sect. 6.

6. Discussion

The lack of accurate distance determinations for the 14 programme stars hinders accurate luminosity determinations, which prevents us from estimating the core masses and from constraining the initial masses. Therefore, the comparison of our abundance results with tailored, state-of-the-art theoretical AGB evolution and nucleosynthetic models is difficult. Given the subsolar metallicities we expect that the majority of the 14 sample stars will have low initial masses ($M \leq 2.0 M_{\odot}$). Future distance determinations will be essential to confirm this assumption.

6.1. Abundance results versus general predictions

In this section, we compare our derived Pb_{up} results with AGB model predictions obtained for a star of $2 M_{\odot}$. The *s*-process in present AGB models is almost insensitive to the initial stellar mass for these low-mass AGB stars.

Different observational indices are commonly used for representing *s*-process distributions and *s*-process overabundances, namely $[ls/Fe]$, $[hs/Fe]$, $[s/Fe]$, and $[hs/ls]$. The elements that are included for the calculation of these indices vary between authors. Here, we calculate the indices with the same elements as in De Smedt et al. (2015, and references therein). For the *ls* index, we take the mean of the relative abundances of Y and Zr. For *hs*, we compute the mean of the relative abundances of La, Ce, Nd, and Sm. The $[hs/Fe]$ and $[ls/Fe]$ of the programme stars are listed in Table 8. The index $[s/Fe]$ is the mean of the relative abundances of the elements for the *ls* and *hs* indices and the index $[hs/ls]$ is calculated according to $[hs/Fe] - [ls/Fe]$. The index $[hs/ls]$ is an indicator of the neutron irradiation when the *s*-process takes place in radiative shells (Gallino et al. 1998; Busso et al. 2001). Larger neutron irradiation results in the creation of

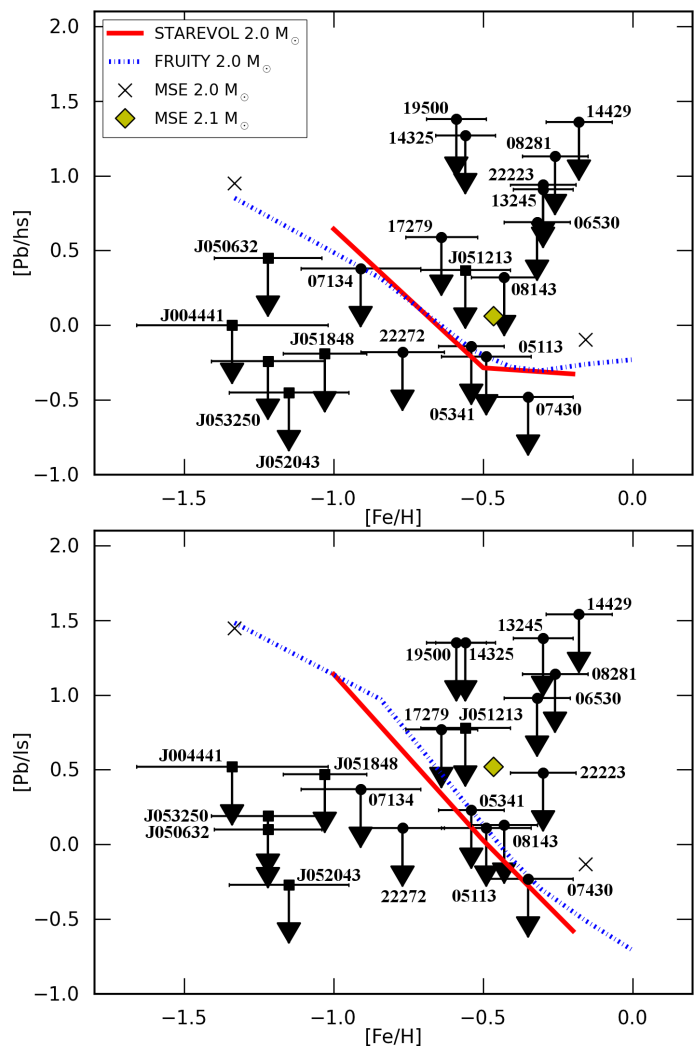


Fig. 14. The observed $[Pb_{up}/hs]$ (upper panel) and the $[Pb_{up}/ls]$ (lower panel) versus $[Fe/H]$ results of the Galactic sample stars of this study (black circles) and the Magellanic Cloud stars in De Smedt et al. (2014, 2015) (black squares). The observed abundance upper limits are plotted together with the $[Pb/hs]$ and $[Pb/ls]$ predictions of the $2.0 M_{\odot}$ STAREVOL models (red full line), the $2.0 M_{\odot}$ and $2.1 M_{\odot}$ Mount Stromlo models (MSE; black crosses and yellow diamond, respectively), and the $2.0 M_{\odot}$ FRUITY models (blue dot-dashed line). The black horizontal lines represent the $[Fe/H]$ uncertainty of the displayed stars. The position of each star from this study is indicated with the first numbers of its IRAS name; the first part of the 2MASS name is used for Magellanic Cloud stars from De Smedt et al. (2014) and De Smedt et al. (2015).

heavier *s*-process elements, hence, $[hs/ls] > 0$. Indices $[Pb/hs]$ ($[Pb/Fe] - [hs/Fe]$) and $[Pb/ls]$ ($[Pb/Fe] - [ls/Fe]$) then represent the overabundance of Pb with respect to the other *s*-process overabundances. The third and second last column of Table 7 show the $[Pb_{up}/hs]$ and $[Pb_{up}/ls]$.

We were unable to determine the abundances of Ce for IRAS 14429-4539 and Sm in four hotter stars. To estimate the Ce and Sm abundances for these objects, we scale the abundances of Ce and Sm to the abundances of La and Nd, which are the elements with an atomic mass closest to Ce and Sm. To scale the abundances, we make use of the AGB nucleosynthesis models from the online database FRUITY³ (Franec Repository of Upgraded Isotopic Tables and Yields; Cristallo et al. (2011)), which covers

³ <http://fruity.oa-teramo.inaf.it/>

Table 7. Pb abundance upper limits Pb_{up} of the programme stars, together with the Pb indices, $[Pb_{up}/hs]$ and $[Pb_{up}/ls]$, and the effective temperature. We adopt the solar Pb abundance of $\log \epsilon(Pb) = 1.75$ dex from Asplund et al. (2009). The abundances of Pb I and Pb II are determined via the 4057.807 Å and 5608.853 Å spectral lines, respectively. The last six rows indicate the Pb_{up} results of six post-AGB stars in the Magellanic Clouds from De Smedt et al. (2014, 2015).

Object	[Fe/H]	$\log \epsilon(PbI_{up})$	$[PbI_{up}/Fe]$	$\log \epsilon(PbII_{up})$	$[PbII_{up}/Fe]$	$[Pb_{up}/hs]$	$[Pb_{up}/ls]$	T_{eff} (K)
IRAS 05113+1347	-0.49	< 2.65	< 1.44			< -0.21	< 0.11	5500
IRAS 05341+0852	-0.54	< 3.15	< 2.10			< -0.14	< 0.23	6750
IRAS 06530-0213	-0.32	< 4.10	< 2.73	< 4.19	< 2.76	< 0.69	< 0.98	7375
IRAS 07134+1005	-0.91	< 2.79	< 2.01			< 0.38	< 0.37	7250
IRAS 07430+1115	-0.31	< 2.50	< 1.07			< -0.48	< -0.23	6000
IRAS 08143-4406 ^a	-0.43	< 3.20	< 1.90			< 0.32	< 0.13	7000
IRAS 08281-4850	-0.26	< 4.20	< 2.74	< 4.20	< 2.71	< 1.13	< 1.14	7875
IRAS 13245-5036	-0.26			< 4.40	< 2.94	< 0.91	< 1.38	9500
IRAS 14325-6428	-0.56			< 3.79	< 2.60	< 1.27	< 1.35	8000
IRAS 14429-4539	-0.64			< 4.40	< 2.83	< 1.36	< 1.54	9375
IRAS 17279-1119	-0.64	< 2.75	< 1.51			< 0.59	< 0.77	7250
IRAS 19500-1709	-0.59	< 3.89	< 2.72			< 1.38	< 1.35	8000
IRAS 22223+4327	-0.30	< 3.25	< 1.82			< 0.94	< 0.48	6500
IRAS 22272+5435	-0.77	< 2.70	< 1.72			< -0.18	< 0.11	5750
J004441.04-732136.4	-1.34	< 3.00	< 2.58			< 0.00	< 0.52	6250
J050632.10-714229.8	-1.22	< 2.05	< 1.52			< 0.45	< 0.10	6750
J052043.86-692341.0	-1.15	< 2.00	< 1.40			< -0.45	< -0.27	5750
J053250.69-713925.8	-1.22	< 2.23	< 1.70			< -0.24	< 0.19	5500
J051213.81-693537.1	-0.56	< 3.30	< 2.11			< 0.37	< 0.78	5875
J051848.86-700246.9	-1.03	< 2.62	< 1.93			< -0.19	< 0.47	6000

^a Determined via the Blue437 spectra of IRAS 08143-4406.

Table 8. Overview of the C/O ratio, the metallicity, and *s*-process indices for our sample of stars.

Object	C/O	[Fe/H]	[ls/Fe]	[hs/Fe]	[s/Fe]	[hs/ls]
IRAS 05113+1347	2.42 ± 0.40	-0.49 ± 0.15	1.33 ± 0.13	1.65 ± 0.07	1.54 ± 0.07	0.32 ± 0.15
IRAS 05341+0852	1.06 ± 0.30	-0.54 ± 0.11	1.87 ± 0.08	2.24 ± 0.06	2.12 ± 0.05	0.37 ± 0.10
IRAS 06530-0213	1.66 ± 0.39	-0.32 ± 0.11	1.75 ± 0.09	2.04 ± 0.08	1.94 ± 0.06	0.29 ± 0.13
IRAS 07134+1005	1.24 ± 0.29	-0.91 ± 0.20	1.64 ± 0.13	1.63 ± 0.20	1.63 ± 0.14	-0.01 ± 0.24
IRAS 07430+1115	1.71 ± 0.30	-0.31 ± 0.15	1.30 ± 0.14	1.55 ± 0.06	1.47 ± 0.06	0.25 ± 0.15
IRAS 08143-4406 ^a	1.66 ± 0.39	-0.43 ± 0.11	1.77 ± 0.08	1.58 ± 0.06	1.65 ± 0.05	-0.19 ± 0.11
IRAS 08281-4850	2.34 ± 0.42	-0.26 ± 0.11	1.57 ± 0.11	1.58 ± 0.12	1.58 ± 0.09	0.01 ± 0.17
IRAS 13245-5036	1.11 ± 0.30	-0.30 ± 0.10	1.56 ± 0.14	2.03 ± 0.11	1.88 ± 0.09	0.47 ± 0.18
IRAS 14325-6428	2.27 ± 0.40	-0.56 ± 0.10	1.25 ± 0.15	1.33 ± 0.19	1.30 ± 0.14	0.08 ± 0.24
IRAS 14429-4539	1.29 ± 0.26	-0.18 ± 0.11	1.29 ± 0.15	1.47 ± 0.10	1.41 ± 0.08	0.18 ± 0.08
IRAS 17279-1119	0.94 ± 0.22	-0.64 ± 0.12	0.74 ± 0.08	0.92 ± 0.09	0.86 ± 0.07	0.18 ± 0.12
IRAS 19500-1709	1.02 ± 0.17	-0.59 ± 0.10	1.37 ± 0.29	1.34 ± 0.30	1.35 ± 0.21	-0.03 ± 0.41
IRAS 22223+4327	1.04 ± 0.22	-0.30 ± 0.11	1.34 ± 0.07	0.88 ± 0.07	1.03 ± 0.05	-0.46 ± 0.10
IRAS 22272+5435	1.46 ± 0.26	-0.77 ± 0.12	1.61 ± 0.08	1.90 ± 0.07	1.80 ± 0.05	0.28 ± 0.11

^a C/O ratio is calculated from the results of the Red580 observations of IRAS 08143-4406; all other results are calculated from the results of the Blue437 observations.

a wide metallicity range, and we use the models with metallicities closest to the metallicity of the star. We use an initial mass of 1.5 M_{\odot} for the FRUITY models.

The [s/Fe] results in Table 8 indeed confirm the strong *s*-process enhancements of the sample stars with [s/Fe] \geq 1.0 except for IRAS 17279-1119 with [s/Fe] = 0.86 dex, which is mildly *s*-process enriched (0.0 < [s/Fe] < 1.0 dex). IRAS 22223+4327 and IRAS 08143-4406 have [hs/ls] < 0. IRAS 07134+1005, IRAS 08281-4850, IRAS 14325-6428, and IRAS 19500-1709 have [hs/ls] \approx 0, while the remaining eight stars, including the mildly enriched IRAS 17279-1119 have [hs/ls] > 0.

The dominant neutron source in low-mass AGB stars is expected to be the $^{13}C(\alpha,n)^{16}O$ reaction during the radiative interpulse phase, leading to [hs/ls] > 0 at subsolar metallicities $-1.2 \text{ dex} \lesssim [Fe/H] \lesssim -0.1 \text{ dex}$ (Goriely & Mowlavi 2000). In intermediate-mass AGB stars ($M > \sim 4 M_{\odot}$), the $^{22}Ne(\alpha,n)^{25}Mg$ reaction within the convective thermal pulse may dominate the neutron production if the temperature at the base of the pulse reaches some 3.5×10^8 K. In this case, the production of light *s*-process elements is favoured because of the convective nature of the region where the neutron irradiation takes place, and the resulting [hs/ls] index tends to be negative (e.g. Goriely & Mowlavi 2000; Goriely & Siess 2004; Karakas et al. 2012).

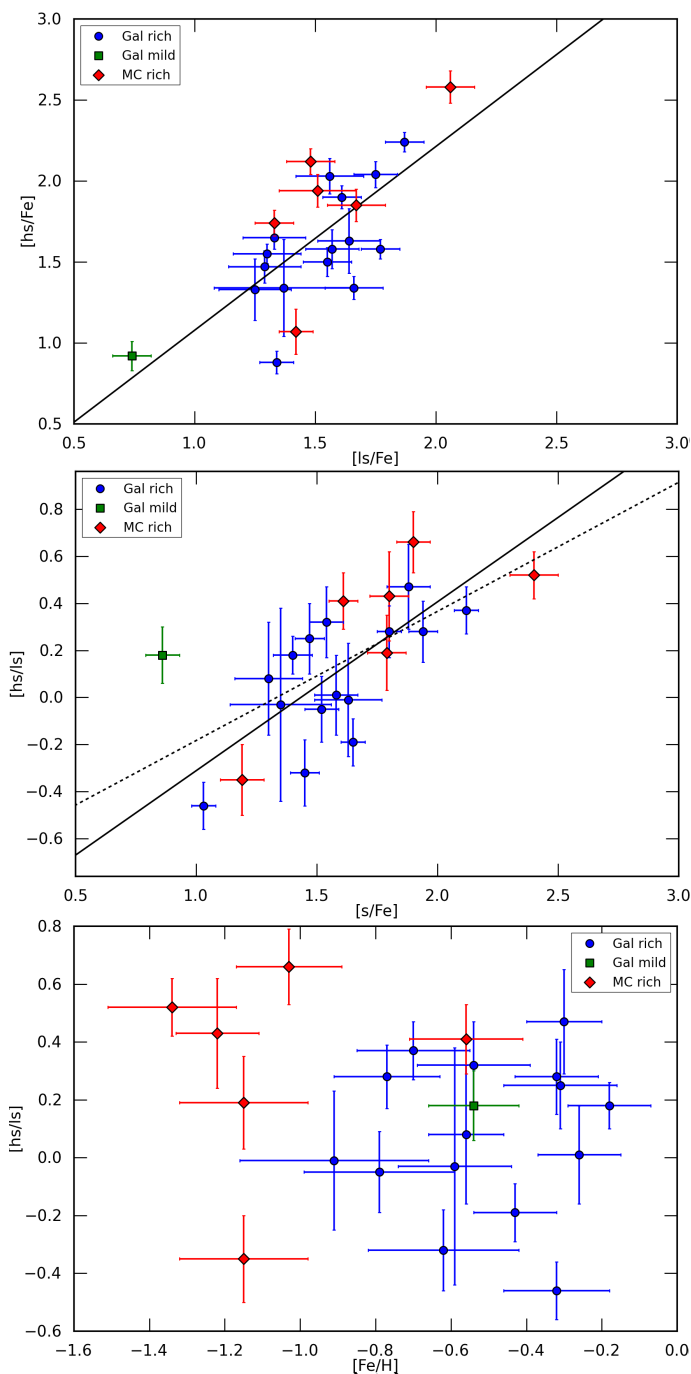


Fig. 15. Upper panel: correlation between the s -process indices $[hs/Fe]$ and $[ls/Fe]$ for our sample stars and Magellanic Cloud stars from De Smedt et al. (2014, 2015). Also included are the results of two Galactic s -process enriched stars from Reyniers et al. (2004): IRAS 04296+3429 and IRAS 23304+6147. Galactic objects are represented by blue circles (= strongly-enriched) and a green square (= mildly-enriched), Magellanic Cloud objects are represented by red diamonds. Middle panel: similar to upper panel but for the correlation between the total enrichment in s -process elements $[s/Fe]$ and the $[hs/ls]$ index. The dashed line shows the least-squares fit to all results, the full line shows the fit for all stars except for IRAS 17279-1119 (green square). Lower panel: similar to upper panel but for the correlation between the metallicity $[Fe/H]$ and the $[hs/ls]$ index. For more information, see text.

In Fig. 14, we compare the adopted Pb_{up} results with the $[Pb/hs]$ and $[Pb/ls]$ predictions of AGB evolution and nucleosynthesis models, as in De Smedt et al. (2015). The determined

abundances are compared to the $2.0 M_{\odot}$ model predictions of the STAREVOL code (Goriely & Siess 2004; Siess 2007, and references therein), the $2.0 M_{\odot}$ and $2.1 M_{\odot}$ Mount-Stromlo Evolutionary (MSE) predictions (Fishlock et al. 2014; Karakas 2010, and references therein), and the $2.0 M_{\odot}$ model predictions of FRUITY (Cristallo et al. 2011). The MSE, STAREVOL, and FRUITY predictions are rather insensitive to the initial stellar mass and show the global expected behaviour of $[Pb/hs]$ and $[Pb/ls]$ as a function of $[Fe/H]$. For the clarity of Fig. 14, we have omitted the $1.5 M_{\odot}$ FRUITY model data since the differences between the $1.5 M_{\odot}$ and $2.0 M_{\odot}$ models are small.

For higher metallicity stars with $[Fe/H] > -0.7$ dex, the model predictions are well within the observed Pb_{up} results, while for stars with $[Fe/H] < -0.7$ dex the discrepancy between observations and predictions become larger as the metallicity decreases. This trend is also confirmed by stars with well-constrained Pb_{up} results, such as IRAS 05113+1347, IRAS 05341+0852, IRAS 06530-0213, and IRAS 22223+4327, covering an $[Fe/H]$ range from -0.8 dex to -0.3 dex. For IRAS 07430+1115, the $[Pb_{up}/hs]$ result falls within the predicted limits.

In addition, it is not surprising to see that the Pb_{up} results of the hottest stars in the sample lie high above the model predictions in Fig. 14. As expected from Fig. 4, the very high Pb_{up} results for these stars are more related to temperature than to visible Pb line features. Therefore, we consider these Pb_{up} as poorly constrained. We conclude that stars with $T_{eff} > 7500$ K without significantly high Pb abundances are not useful for comparison with theoretical Pb abundance predictions. However, these hot stars remain useful for C/O ratio and other s -element comparisons.

6.2. Correlations

Previous studies (e.g. Van Winckel 2003) have shown that there is no correlation between metallicity and neutron irradiation. According to the models, the $[hs/ls]$ index is expected to increase with decreasing metallicity up to $[Fe/H] \sim -0.4$ dex after which it strongly decreases towards higher metallicities (e.g. Goriely & Mowlavi 2000). With the addition of our new results, we confirm that this is not observed: in the lower panel of Fig. 15, we illustrate the absence of this expected correlation between metallicity and $[hs/ls]$. This implies that the total neutron irradiation is not (only) dependent on metallicity in our metallicity range.

In the upper panel of Fig. 15, we show the correlation between $[hs/Fe]$ and $[ls/Fe]$ for our sample stars, the Magellanic Cloud post-AGB stars in van Aarle et al. (2013); De Smedt et al. (2014, 2015), and for two additional Galactic s -process enriched post-AGB stars from Reyniers et al. (2004). It is clear that both s -process indices are correlated and a high $[ls/Fe]$ generally also implies a strong enhancement in $[hs/Fe]$. The spread is, however, large and this indicates that the different objects were subject to a variable neutron irradiation, irrespective of the dilution of the atmosphere.

In previous studies, Reyniers et al. (2004), van Aarle et al. (2013), and in De Smedt et al. (2015) identified a strong correlation between $[s/Fe]$ and the $[hs/ls]$ index in Galactic and Magellanic Cloud objects. Strongly enriched objects, for which there has been a low dilution of the enriched material with the envelope material, were also subject to strong neutron irradiation and, hence, showed a high $[hs/ls]$. Here, we add/update the results of our 14 programme stars to the previously used sample. The resulting $[s/Fe]$ and $[hs/ls]$ correlation is shown in the middle panel of Fig. 15 where two correlations are shown. The dashed line represents the correlation between the $[s/Fe]$ vs $[hs/ls]$ results

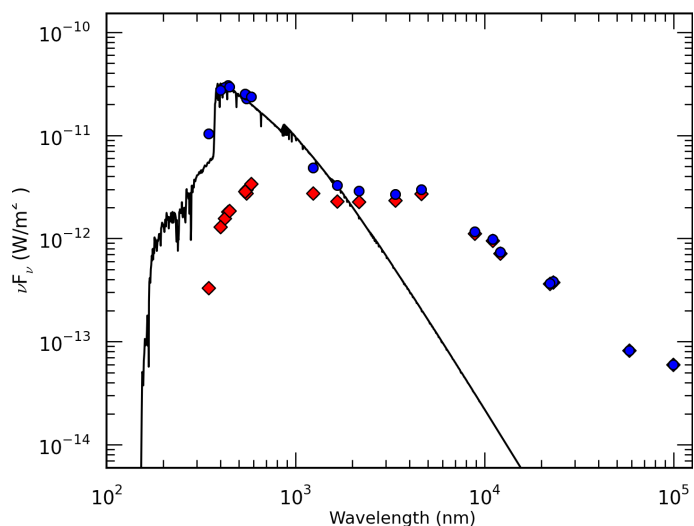


Fig. 16. Spectral energy distribution of IRAS 17279-1119. Red dots represent the red, original photometry, blue dots represent the dereddened photometry. The black line is the scaled Kurucz atmosphere model.

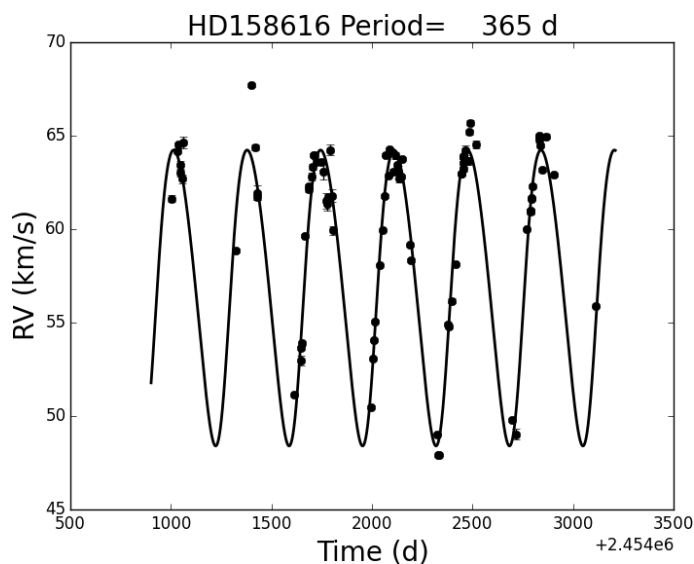


Fig. 17. Radial velocity orbit of IRAS 17279-1119. Black dots represent the observed radial velocities; the black curve is the sine-fit to the orbit. For more information, see text.

for all stars in the plot; the full line represents the correlation without the inclusion of IRAS 17279-1119. We choose these two correlations as IRAS 17279-1119 has $[s/Fe] < 1$ dex whereas the other stars have $[s/Fe] \geq 1$ dex. The correlation of the full and dashed lines in the middle panel of Fig. 15 are 0.75 and 0.65, respectively. The second result shows that the inclusion of the mildly enhanced IRAS 17279-1119 moderately lowers the correlation for all objects. This suggests a different *s*-process history for IRAS 17279-1119 with respect to the other programme stars (see Sect. 7).

7. IRAS 17279-1119

IRAS 17279-1119 has only a mild *s*-process enrichment (see lower right panel of Fig. 9) and is an outlier in the middle panel of Fig. 15, so in this section we focus specifically on this object.

Fig. 16 shows the spectral energy distribution (SED) of IRAS 17279-1119. The photometric data for constructing the SED

Table 9. Orbital elements of IRAS 17279-1119.

		σ
Period (d)	365.0	1.0
<i>e</i>	0.0 (forced)	
<i>K</i> (km s ⁻¹)	7.92	0.44
γ (km s ⁻¹)	56.8	0.5
<i>a</i> sin <i>i</i> (A.U.)	0.27	0.02
<i>f</i> (M) (M_{\odot})	0.026	0.004
RMS residuals (km s ⁻¹)	1.8	

is retrieved from the following catalogues: the General Catalogue of Photometric Data (GCPD; Mermilliod et al. 1997), the All-sky compiled catalogue of 2.5 million stars (Kharchenko 2001), the 2MASS All-Sky Catalog of Point Sources (Cutri et al. 2003), the WISE All-Sky Data catalogue (Cutri et al. 2012), the AKARI/IRC mid-infrared all-sky survey (Ishihara et al. 2010), and the IRAS catalogue of Point Sources (Helou & Walker 1988).

Fig. 16 shows both the original raw photometric points (red diamonds) as well as the dereddened data (blue dots). We consider two possible reddening sources for Galactic objects. The first source is reddening by interstellar dust in the Galaxy towards IRAS 17279-1119. The second source is reddening by the circumstellar dust of IRAS 17279-1119 itself. We use the Galactic extinction curves of Cardelli et al. (1989) to determine the reddening for both sources. The total reddening is determined by applying a χ^2 minimisation on the fit between the dereddened broadband fluxes and our preferred Kurucz model atmosphere, which we used for the abundance study of IRAS 17279-1119. The error on the total reddening $E(B-V)$ is determined by a Monte Carlo simulation of 100 arrays with a normal distribution of the original flux. We find a total reddening of $E(B-V) = 0.76 \pm 0.02$ for IRAS 17279-1119.

The SED shown in Fig. 16 indicates an excess starting at 2 micron indicating the thermal emission of dust near the dust-sublimation temperature and therefore close to the central star. It is now well established that this traces the presence of a stable compact circumbinary disc (e.g. De Ruyter et al. 2006; Deroo et al. 2007; Gielen et al. 2011; Hillen et al. 2013, 2015; Bujarrabal et al. 2015; Gezer et al. 2015). The specific characteristics of the SED are closely related to the binary nature of the central star (Van Winckel et al. 2009).

We obtained radial velocity monitoring data with the HERMES spectrograph (Raskin et al. 2011) mounted on the 1.2 meter Mercator telescope in the framework of our large programme on evolved binaries (Van Winckel et al. 2010; Gorlova et al. 2013). In total we obtained 85 radial velocity measurements starting on 19/06/2009 covering a total time span of 2211d. We also used the ASAS (Pojmanski & Maciejewski 2004) photometry to study the photometric behaviour. The photometry consists of 788 data points covering a time span of 3156d. Many of the variables near the Population II Cepheid instability strip have complex light curves in which several modes are excited with periods close to each other so that beating effects are easily detectable (Kiss et al. 2006). IRAS 17279-1119 is no exception and periods of 90, 87, and 83 days are found in the photometry using a S/N criterion of 4 in the Fourier transform. Unfortunately, our photometric series do not overlap in time with the radial velocity series.

We detect orbital motion (see Fig 17) with an orbital period of exactly one year. The orbital solution is clear with a fractional variance reduction of 91% in the fit. In Table 9 we list the orbital data. We cover in total close to six cycles, but as the period is

close to one year, the phase coverage is not ideal. Nonetheless, the orbital detection is clear.

With an 'a sin *i*' of only 0.27 AU, it is clear that the current orbit is too small to accommodate a TP-AGB star whose radius is expected to be 1-2 AU. The object must have experienced strong binary interaction when on the AGB. The mass function gives a constraint on the mass of the companion provided the mass of the primary and the inclination are known. As the primary is a post-AGB star, it is fair to assume the mass is a typically white dwarf mass of 0.6 M_{\odot} . Assuming a most probable inclination of 60 degrees, the mass of the companion is only 0.3 M_{\odot} . With an inclination of 30 degrees, this becomes 0.6 M_{\odot} . As there are no symbiotic activities, we suggest that the companion is non-evolved.

To our knowledge, IRAS 17279-1119 is the first *s*-process rich post-AGB star discovered to be in a spectroscopic binary. If, during the binary interaction phase, there was mass transfer of enriched material to the secondary, the companion accreted *s*-process rich gas. This object seems therefore a precursor of extrinsically *s*-process enriched stars. These are binaries in which the observed *s*-process rich component was polluted by material expelled from their companion stars when they passed the AGB evolutionary phase and which are now white dwarfs (see Jorissen et al. 1998). IRAS 17279-1119 may very well be the first detected precursor of Ba dwarfs, given the low mass of the companion.

8. Conclusions

In this paper, we presented a homogeneous abundance study of a sample of 14 Galactic *s*-process enriched post-AGB stars with the aim of determining Pb abundances. Our results confirm that two newly identified 21 μm sources, IRAS 13245-5036 and IRAS 14429-4539, are indeed carbon and *s*-process enriched and we confirm the post-AGB nature of both objects. Furthermore, we find a strong chemical diversity for the sample stars, ranging from only a mild *s*-process enrichment up to strong *s*-process enrichment.

None of the sample objects display clear distinctive Pb lines in their spectra and therefore we can only determine Pb abundance upper limits (Pb_{up}). These Pb abundance upper limits are determined using synthetic spectra. A comparison with theoretical spectra reveals that some of the cooler stars in the sample display visible contributions of Pb in the unresolved blends. Because of the low S/N, it is impossible to determine the contribution and hence abundance accurately.

For the hotter stars with $T_{\text{eff}} > 7500$ K, there are no visible Pb line contributions in the spectra. Therefore, these Pb_{up} results are poorly constrained, which makes hot post-AGB stars without drastically high Pb abundances not useful for the Pb comparison with theoretical AGB nucleosynthesis predictions.

A comparison of observed Galactic Pb_{up} abundances with theoretical *s*-process calculations of $\sim 2.0 M_{\odot}$ stellar models confirm the results of Magellanic Cloud stars from De Smedt et al. (2014) and De Smedt et al. (2015). For metallicities $[\text{Fe}/\text{H}] > -0.7$ dex, the predicted Pb abundances are well within the observed Pb_{up} results, while there exists an increasing discrepancy towards lower metallicities. Additional research is necessary to explain this trend.

We confirm that there is no correlation between neutron irradiation and metallicity in the metallicity range probed here. These results show that a wide spread in neutron irradiation is needed at all metallicities to explain these results. In comparative studies of extrinsically *s*-process enhanced objects, similar

conclusions were obtained, even at lower metallicity (e.g. Bisterzo et al. 2012).

We confirm the correlation between $[\text{hs}/\text{ls}]$ and $[\text{s}/\text{Fe}]$ indicating the connection between strong neutron irradiation and overall photospheric enrichments. The mildly *s*-process enriched IRAS 17279-1119 does not follow this correlation because the orbital elements suggest that an evolutionary cut-off from the AGB was forced prematurely because of binary interaction: the current orbit is too small to accommodate an AGB star with a typical luminosity. In addition, IRAS 17279-1119 is to our knowledge the first confirmed *s*-process rich post-AGB star in a binary system.

In summary, we find an increasing discrepancy between observed and predicted Pb abundances towards lower metallicities. All objects with a metallicity $[\text{Fe}/\text{H}] < -0.7$ dex show Pb upper limits that are lower than the predicted Pb abundances. Contrary to the Magellanic Cloud samples, the distances to the Galactic sample stars are poorly known and hence it is difficult to constrain their current core masses and their initial masses. Distance estimates are hence necessary to connect the determined abundance results with tailored theoretical predictions in detail. The GAIA distance determinations will be crucial in this respect.

Acknowledgements. The authors thank S. Cristallo for the public availability of the FRUITY models. KDS, HVW, RM, and DK acknowledge support of the KU Leuven contract GOA/13/012. DK acknowledges support of the FWO grant G.OB86.13. SG and LS are FNRS research associates. AIK was supported through an Australian Research Council Future Fellowship (FT110100475). Based on observations obtained with the HERMES spectrograph, which is supported by the Research Foundation - Flanders (FWO), Belgium, the Research Council of KU Leuven, Belgium, the Fonds National de la Recherche Scientifique (F.R.S.-FNRS), Belgium, the Royal Observatory of Belgium, the Observatoire de Genève, Switzerland and the Thüringer Landessternwarte Tautenburg, Germany.

References

- Abia, C., de Laverny, P., & Wahlin, R. 2008, *A&A*, 481, 161
 Abia, C., Domínguez, I., Gallino, R., et al. 2002, *ApJ*, 579, 817
 Aoki, W., Ryan, S. G., Norris, J. E., et al. 2001, *ApJ*, 561, 346
 Asplund, M., Grevesse, N., Sauval, A. J., & Scott, P. 2009, *ARA&A*, 47, 481
 Behara, N. T., Bonifacio, P., Ludwig, H.-G., et al. 2010, *A&A*, 513, A72
 Bisterzo, S., Gallino, R., Straniero, O., Cristallo, S., & Käppeler, F. 2010, *MNRAS*, 404, 1529
 Bisterzo, S., Gallino, R., Straniero, O., Cristallo, S., & Käppeler, F. 2012, *MNRAS*, 422, 849
 Bujarrabal, V., Castro-Carrizo, A., Alcolea, J., & Van Winckel, H. 2015, *A&A*, 575, L7
 Busso, M., Gallino, R., Lambert, D. L., Travaglio, C., & Smith, V. V. 2001, *ApJ*, 557, 802
 Cardelli, J. A., Clayton, G. C., & Mathis, J. S. 1989, *ApJ*, 345, 245
 Castelli, F. & Kurucz, R. L. 2004, *ArXiv astro-ph/0405087* [[arXiv:astro-ph/0405087](https://arxiv.org/abs/astro-ph/0405087)]
 Cerrigone, L., Hora, J. L., Umana, G., et al. 2011, *ApJ*, 738, 121
 Cristallo, S., Piersanti, L., Straniero, O., et al. 2011, *ApJS*, 197, 17
 Cutri, R. M., Skrutskie, M. F., van Dyk, S., et al. 2003, *VizieR Online Data Catalog*, 2246, 0
 Cutri, R. M., Wright, E. L., Conrow, T., et al. 2012, *Explanatory Supplement to the WISE All-Sky Data Release Products*, Tech. rep.
 De Ruyter, S., Van Winckel, H., Maas, T., et al. 2006, *A&A*, 448, 641
 De Smedt, K., Van Winckel, H., Kamath, D., et al. 2014, *A&A*, 563, L5
 De Smedt, K., Van Winckel, H., Kamath, D., & Wood, P. R. 2015, *A&A*, 583, A56
 De Smedt, K., Van Winckel, H., Karakas, A. I., et al. 2012, *A&A*, 541, A67
 Dekker, H., D'Odorico, S., Kaufer, A., Delabre, B., & Kotzlowski, H. 2000, in *Society of Photo-Optical Instrumentation Engineers (SPIE) Conference Series*, Vol. 4008, Society of Photo-Optical Instrumentation Engineers (SPIE) Conference Series, ed. M. Iye & A. F. Moorwood, 534-545
 Deroo, P., Acke, B., Verhoelst, T., et al. 2007, *A&A*, 474, L45
 Deroo, P., Reyniers, M., Van Winckel, H., Goriely, S., & Siess, L. 2005, *A&A*, 438, 987
 Fishlock, C. K., Karakas, A. I., Lugaro, M., & Yong, D. 2014, *ApJ*, 797, 44

- Gallino, R., Arlandini, C., Busso, M., et al. 1998, *ApJ*, 497, 388
- Gezer, I., Van Winckel, H., Bozkurt, Z., et al. 2015, *MNRAS*, 453, 133
- Gielen, C., Bouwman, J., van Winckel, H., et al. 2011, *A&A*, 533, A99
- Goriely, S. & Mowlavi, N. 2000, *A&A*, 362, 599
- Goriely, S. & Siess, L. 2004, *A&A*, 421, L25
- Gorlova, N., Van Winckel, H., Vos, J., et al. 2013, in *EAS Publications Series*, Vol. 64, *EAS Publications Series*, ed. K. Pavlovski, A. Tkachenko, & G. Torres, 163–170
- Helou, G. & Walker, D. W., eds. 1988, *Infrared astronomical satellite (IRAS) catalogs and atlases. Volume 7: The small scale structure catalog*, Vol. 7
- Hillen, M., Menu, J., de Vries, B. L., et al. 2015, in *Astronomical Society of the Pacific Conference Series*, Vol. 497, *Why Galaxies Care about AGB Stars III: A Closer Look in Space and Time*, ed. F. Kerschbaum, R. F. Wing, & J. Hron, 175
- Hillen, M., Verhoelst, T., Van Winckel, H., et al. 2013, *A&A*, 559, A111
- Hrivnak, B. J., Volk, K., & Kwok, S. 2009, *ApJ*, 694, 1147
- Ishihara, D., Onaka, T., Katata, H., et al. 2010, *A&A*, 514, A1
- Jorissen, A., Van Eck, S., Mayor, M., & Udry, S. 1998, *A&A*, 332, 877
- Kamath, D., Wood, P. R., & Van Winckel, H. 2014, *MNRAS*, 439, 2211
- Kamath, D., Wood, P. R., & Van Winckel, H. 2015, *MNRAS*, 454, 1468
- Karakas, A. I. 2010, *MNRAS*, 403, 1413
- Karakas, A. I., García-Hernández, D. A., & Lugaro, M. 2012, *ApJ*, 751, 8
- Karakas, A. I. & Lattanzio, J. C. 2014, *PASA*, 31, 30
- Kharchenko, N. V. 2001, *Kinematika i Fizika Nebesnykh Tel*, 17, 409
- Kiselman, D. 2002, *Highlights of Astronomy*, 12, 429
- Kiss, L. L., Szabó, G. M., & Bedding, T. R. 2006, *MNRAS*, 372, 1721
- Kobayashi, C., Karakas, A. I., & Umeda, H. 2011, *MNRAS*, 414, 3231
- Kupka, F., Piskunov, N., Ryabchikova, T. A., Stempels, H. C., & Weiss, W. W. 1999, *A&AS*, 138, 119
- Kwok, S., Volk, K. M., & Hrivnak, B. J. 1989, *ApJ*, 345, L51
- Lugaro, M., Campbell, S. W., Van Winckel, H., et al. 2015, *A&A*, 583, A77
- Lugaro, M., Karakas, A. I., Stancliffe, R. J., & Rijs, C. 2012, *ApJ*, 747, 2
- Lyubimkov, L. S., Lambert, D. L., Korotin, S. A., et al. 2011, *MNRAS*, 410, 1774
- Mermilliod, J.-C., Mermilliod, M., & Hauck, B. 1997, *A&AS*, 124, 349
- Mowlavi, N., Jorissen, A., & Arnould, M. 1998, *A&A*, 334, 153
- Neyskens, P., van Eck, S., Jorissen, A., et al. 2015, *Nature*, 517, 174
- Pojmanski, G. & Maciejewski, G. 2004, *Acta Astron.*, 54, 153
- Rao, S. S., Giridhar, S., & Lambert, D. L. 2012, *MNRAS*, 419, 1254
- Raskin, G., van Winckel, H., Hensberge, H., et al. 2011, *A&A*, 526, A69
- Reddy, B. E., Bakker, E. J., & Hrivnak, B. J. 1999, *ApJ*, 524, 831
- Reddy, B. E., Lambert, D. L., Gonzalez, G., & Yong, D. 2002, *ApJ*, 564, 482
- Reyniers, M. 2002, PhD thesis, Departement Natuurkunde en Sterrenkunde, K.U.Leuven, Celestijnenlaan 200B, 3001 Leuven, Belgium
- Reyniers, M., Abia, C., Van Winckel, H., et al. 2007a, *A&A*, 461, 641
- Reyniers, M., van de Steene, G. C., van Hoof, P. A. M., & van Winckel, H. 2007b, *A&A*, 471, 247
- Reyniers, M., Van Winckel, H., Gallino, R., & Straniero, O. 2004, *A&A*, 417, 269
- Romano, D., Karakas, A. I., Tosi, M., & Matteucci, F. 2010, *A&A*, 522, A32
- Siess, L. 2007, *A&A*, 476, 893
- Snedden, C. A. 1973, PhD thesis, The University of Texas at Austin.
- Straniero, O., Gallino, R., Busso, M., et al. 1995, *ApJ*, 440, L85
- van Aarle, E., Van Winckel, H., De Smedt, K., Kamath, D., & Wood, P. R. 2013, *A&A*, 554, A106
- van Aarle, E., van Winckel, H., Lloyd Evans, T., et al. 2011, *A&A*, 530, A90
- Van Eck, S., Goriely, S., Jorissen, A., & Plez, B. 2001, *Nature*, 412, 793
- Van Eck, S., Goriely, S., Jorissen, A., & Plez, B. 2003, *A&A*, 404, 291
- Van Winckel, H. 2003, *ARA&A*, 41, 391
- Van Winckel, H., Jorissen, A., Gorlova, N., et al. 2010, *MemSAI*, 81, 1022
- Van Winckel, H., Lloyd Evans, T., Briquet, M., et al. 2009, *A&A*, 505, 1221
- Van Winckel, H. & Reyniers, M. 2000, *A&A*, 354, 135

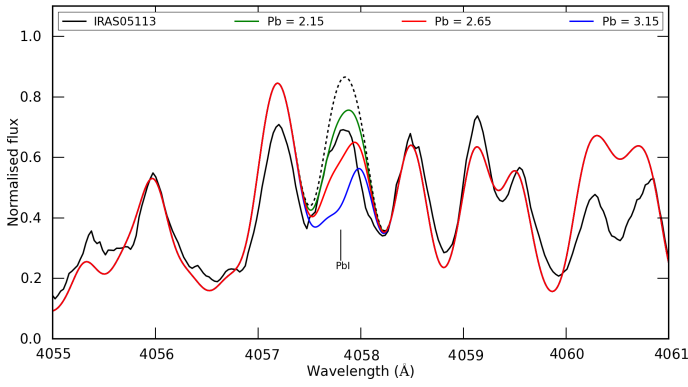


Fig. A.1. Spectrum synthesis of the Pb I line at 4057.807 Å for IRAS 05113+1347. The black spectrum is the observed UVES spectrum; the coloured spectra represent synthetic spectra with different Pb abundances. The red line represents the adopted Pb abundance upper limit; the green and blue lines represent the adopted abundance upper limit -0.5 dex and $+0.5$ dex, respectively. The dashed black line shows the synthetic spectrum if no Pb is present.

Appendix A: Pb abundances of individual stars

In this appendix, we give an overview of the Pb abundance upper limit determinations for the different programme stars together with a brief discussion of the Pb_{up} results.

Appendix A.1: IRAS 05113+1347

The Pb abundance upper limit determination of IRAS 05113+1347 is presented in Fig. A.1. The determination of the continuum is difficult as the region is dominated by large spectral blends. We use the spectral lines at 4057.5 and 4058.2 Å to optimally estimate the position of the continuum. Thereafter, we adopted a Pb abundance upper limit, which fully incorporates the line feature at 4057.807 Å.

The adopted Pb_{up} of IRAS 05113+1347 results in a $[Pb_{up}/Fe]$ which is about 0.2 dex lower than the value for $[hs/Fe]$ (left upper panel of Fig. 8) and similar to the element-over-iron ratios of the elements beyond the Ba-peak.

Appendix A.2: IRAS 05341+0852

For the strongly s -process enriched IRAS 05341+0852, we estimate the position of the continuum by finding a compromise between the spectral blends at 4057.5 and 4058.2 Å in Fig. A.2. We adopt a Pb abundance upper limit, which fully includes the small visible line feature.

Although it is one of the most s -process enriched Galactic post-AGB stars studied to date, IRAS 05341+0852 displays a $[Pb_{up}/Fe]$ that is about 0.15 dex lower than $[hs/Fe]$ (middle upper panel of Fig. 8). Like in IRAS 05113+1347, the $[Pb_{up}/Fe]$ seems similar to the element-over-iron ratios of the elements beyond the Ba-peak.

Appendix A.3: IRAS 06530-0213

The Pb abundance determination of IRAS 06530-0213 is described in detail in Sect. 5. The spectral synthesis of the Pb regions are depicted in Fig. 12. We use the Pb_{up} result of the Pb I line for this strongly s -process enriched post-AGB star. The resulting $[Pb_{up}/Fe]$ is about 0.7 dex higher than $[hs/Fe]$ (left upper

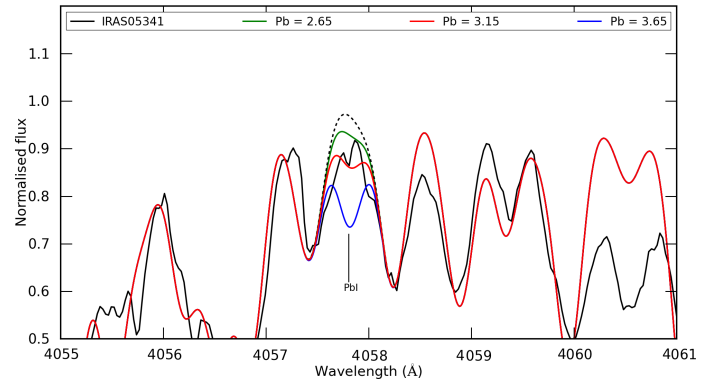


Fig. A.2. Spectrum synthesis of the Pb I line at 4057.807 Å for the UVES spectrum of IRAS 05341+0852. Lines and symbols are similar to Fig. A.1.

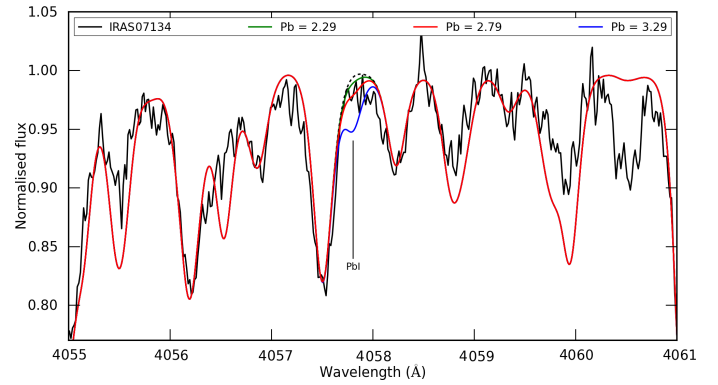


Fig. A.3. Spectrum synthesis of the Pb I line at 4057.807 Å for the HERMES spectrum of IRAS 07143+1005. Lines and symbols are similar to Fig. A.1.

panel of Fig. 9) and the element-over-iron ratios of the elements beyond the Ba-peak.

Appendix A.4: IRAS 07143+1005

We estimate the position of the continuum of IRAS 07143+1005 using the spectral blends at 4056.2, 4056.9 and 4057.5 Å at the blue side of the Pb I line, and the blends at 4058.2 and 4059.3 Å at the red side of the Pb I line in Fig. A.3. The spectral region of the Pb I line is dominated by noise and we cannot detect any visible contribution from the Pb line. We therefore adopt a Pb abundance upper limit, which includes the noise at 4057.807 Å.

The adopted $[Pb_{up}/Fe]$ is about 0.4 dex higher than $[hs/Fe]$ and $[ls/Fe]$, which are both similar in enrichment (middle upper panel of Fig. 9).

Appendix A.5: IRAS 07430+1115

In Fig. A.4, we use the spectral blends at 4057.5 and 4058.8 Å to estimate the position of the continuum. Although not clearly visible, the synthetic spectrum without the Pb I line suggests a possible small contribution of Pb at 4057.807 Å. Therefore, we adopt a Pb abundance upper limit that incorporates the peak of the Pb I line feature.

The adopted Pb_{up} of IRAS 07430+1115 gives a $[Pb_{up}/Fe]$, which is significantly lower than $[hs/Fe]$ with a difference of about 0.5 dex (right upper panel of Fig. 8).

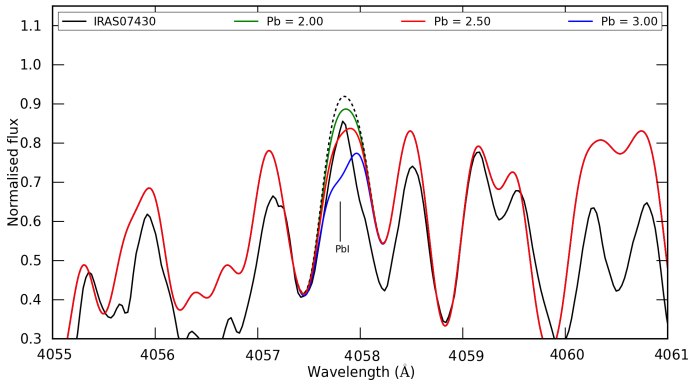


Fig. A.4. Spectrum synthesis of the Pb I line at 4057.807 Å for the UVES spectrum of IRAS 07430+1115. Lines and symbols are similar to Fig. A.1.

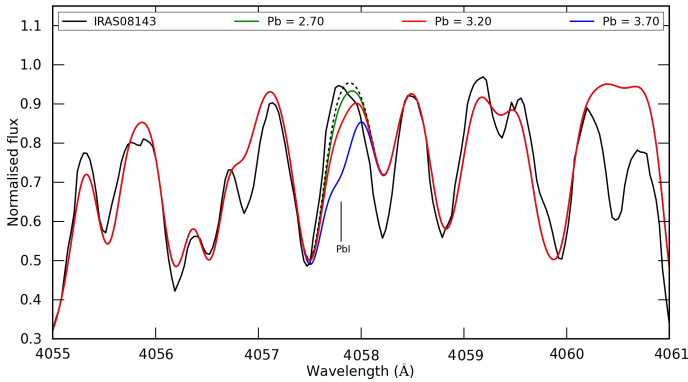


Fig. A.5. Spectrum synthesis of the Pb I line at 4057.807 Å for the BLUE437 UVES spectrum of IRAS 08143-4406. Lines and symbols are similar to Fig. A.1.

Appendix A.6: IRAS 08143-4406

The position of the continuum for IRAS 08143-4406 is estimated using the spectral blends at 4057.5 and 4058.8 Å in Fig. A.5. The spectrum of IRAS 08143-4406 does not show visible contribution of Pb at 4057.807 Å, and we see that with the estimated continuum position, the spectral feature at the blue side of the Pb I line is not even contained within the boundaries of the synthetic spectrum without Pb I line, which could possibly be attributed to noise. As a result of these uncertainties, we adopt a Pb abundance upper limit that fully incorporates the spectral line in the spectral region of the Pb I line.

We find that $[\text{Pb}_{\text{up}}/\text{Fe}]$ is about 0.1 higher than $[\text{ls}/\text{Fe}]$ and 0.3 dex higher than $[\text{hs}/\text{Fe}]$, respectively (right upper panel of Fig. 9).

Appendix A.7: IRAS 08281-4850

The spectra of IRAS08281-4850 reveal possible Pb line features in both panels of Fig. A.6, but we assume these features are more likely due to noise than a real abundance of Pb. Nevertheless, we adopt a similar Pb abundance upper limit for both Pb lines that fully incorporates the visible spectral features. For the Pb I line, we use the spectral blends at 4056.2, 4057.5, and 4058.8 Å to estimate the position of the continuum. For the Pb II line, we see unidentified spectral lines at 5606.7 and 5607 Å and also at both sides of the Pb II line. These spectral lines are not included in the linelists and we can only use the continuum in the region 5606 -

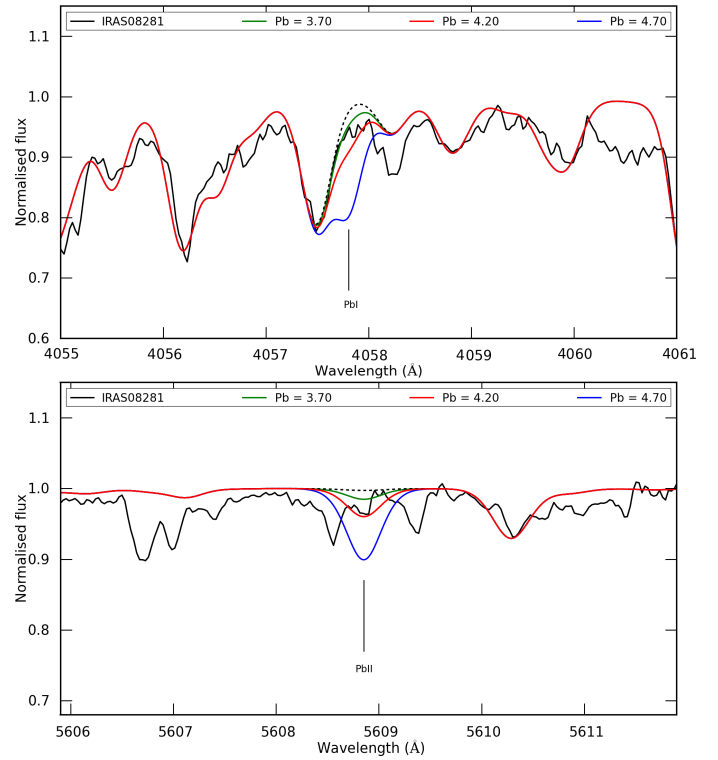


Fig. A.6. Spectrum synthesis of the Pb I line at 4057.807 Å (upper panel) and the Pb II line at 5608.853 Å (lower panel) for the UVES spectra of IRAS 08281-4850. Lines and symbols are similar to Fig. A.1.

5606.5 Å and 5611.5 - 5612 Å, in combination with the spectral line at 5610.2 Å, to estimate the continuum position.

We find a similar Pb_{up} for both the Pb I and Pb II lines. This results in a $[\text{Pb}_{\text{up}}/\text{Fe}]$ that is about 1.2 dex higher than the $[\text{hs}/\text{Fe}]$ and $[\text{ls}/\text{Fe}]$ (left lower panel of Fig. 9).

Appendix A.8: IRAS 13245-5036

The Pb abundance determination of IRAS 13245-5036 is described in detail in Sect. 5. The spectral synthesis of the Pb II region is depicted in Fig. 13. For this hottest star in the sample, we only use the Pb II line to determine Pb_{up} . The adopted $[\text{Pb}_{\text{up}}/\text{Fe}]$ is about 0.9 dex higher than $[\text{hs}/\text{Fe}]$ (left upper panel of Fig. 10).

Appendix A.9: IRAS 14325-6428

The Pb II line spectral region of IRAS 14325-6428 is dominated by noise and does not show a visible Pb line contribution in Fig. A.7. We estimate the position of the continuum by fitting to the average continuum in the shown spectral region. Around 5610.2 Å, a small line appears in the synthetic spectra that is not present in the observed spectra, so we do not use this line for the continuum estimate. We then adopt a Pb abundance upper limit, which incorporates the continuum at 5608.853 Å.

The adopted $[\text{Pb}_{\text{up}}/\text{Fe}]$ is only determined via the Pb II line, and is about 1.3 dex higher than $[\text{hs}/\text{Fe}]$ (right upper panel of Fig. 10).

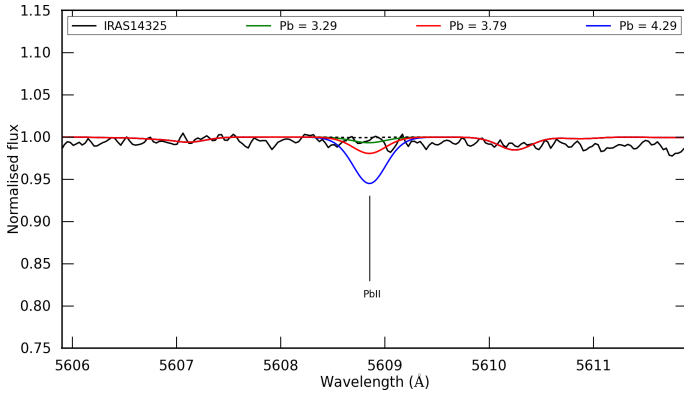


Fig. A.7. Spectrum synthesis of the Pb II line at 5608.853 Å for the UVES spectrum of IRAS 14325-6428. Lines and symbols are similar to Fig. A.1.

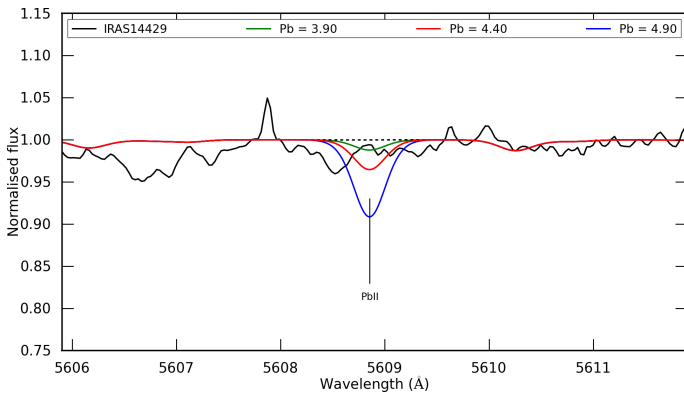


Fig. A.8. Spectrum synthesis of the Pb II line at 5608.853 Å for the UVES spectrum of IRAS 14429-4539. Lines and symbols are similar to Fig. A.1.

Appendix A.10: IRAS 14429-4539

Fig. A.8 shows that the spectral region of the Pb II at 5608.853 Å of IRAS 14429-4539 is totally dominated by noise and that there is no visible contribution of the Pb line. There is a visible line in the spectrum at 5606.6 Å, but it is not clear whether this feature is real or due to noise. For this reason, it is not included in the linelists. We therefore estimate the position of the continuum by fitting the average continuum in the shown spectral region. We then adopt a Pb abundance upper limit, which incorporates the estimated continuum at 5608.853 Å.

For the second hottest star in the sample, we only use the Pb II line for the Pb_{up} determination. $[Pb_{up}/Fe]$ exceeds $[hs/Fe]$ by almost 1.4 dex (left lower panel of Fig. 10).

Appendix A.11: IRAS 17279-1119

The mildly IRAS 17279-1119 does not show any visible Pb line features in Fig. A.9. The local continuum is estimated using the spectral blends at 4056.2, 4057.5 and 4058.2 Å. We adopt a Pb abundance upper limit, which fully incorporates the spectral region at 4057.807 Å.

The $[Pb_{up}/Fe]$ for the mildly *s*-process enriched post-AGB star IRAS 17279-1119 is 0.6 dex higher than $[hs/Fe]$ (right lower panel of Fig. 9).

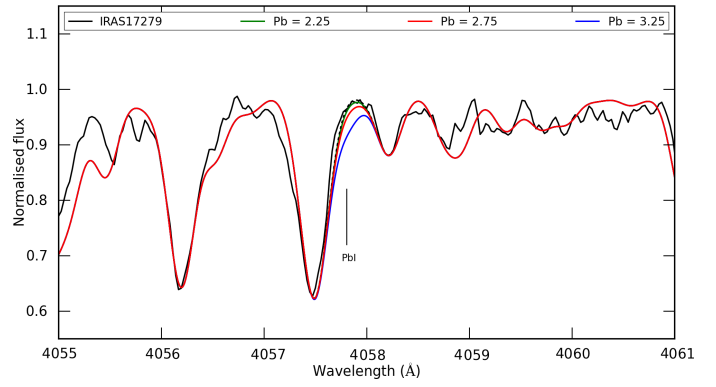


Fig. A.9. Spectrum synthesis of the Pb I line at 4057.807 Å for the UVES spectrum of IRAS 17279-1119. Lines and symbols are similar to Fig. A.1.

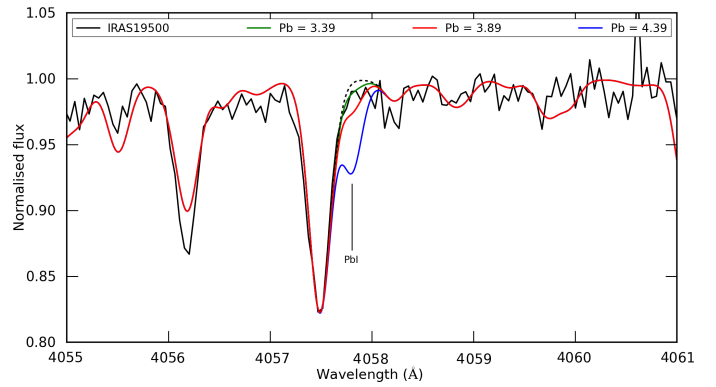


Fig. A.10. Spectrum synthesis of the Pb I line at 4057.807 Å for the HERMES spectrum of IRAS 19500-1709. Lines and symbols are similar to Fig. A.1.

Appendix A.12: IRAS 19500-1709

For the atmospheric parameter set of IRAS 19500-1709 to appear, the Pb I line at 4057.807 Å requires a lower Pb abundance than the Pb II line at 5608.853 Å. Therefore, we only use the Pb I line for our analysis. Fig. A.10 shows that the spectral region of the Pb I line has a poor S/N. We use the spectral blend at 4057.5 Å to estimate the position of the continuum and then adopt a Pb abundance upper limit, which fully incorporates the noise at 4057.807 Å.

For IRAS 19500-1709, $[hs/ls] \approx 0$ and the derived $[Pb_{up}/Fe]$ is about 1.35 dex higher than $[ls/Fe]$ and $[hs/Fe]$ (right lower panel of Fig. 10).

Appendix A.13: IRAS 22223+4327

The Pb abundance determination of IRAS 22223+4327 is described in detail in Sect. 5. The spectral synthesis of the Pb I region is depicted in Fig. 11. For IRAS 22223+4327, the adopted Pb_{up} results in a $[Pb_{up}/Fe]$, which lies about 1.0 dex above $[hs/Fe]$ (left lower panel of Fig. 8). For IRAS 22223+4327, the ls elements have higher enrichments than the hs elements and our estimate for $[Pb_{up}/Fe]$ lies about 0.5 dex above $[ls/Fe]$.

Appendix A.14: IRAS 22272+5435

The spectral region of the Pb I line for IRAS 22272+5435 is dominated by strong blends in combination with low S/N in Fig.

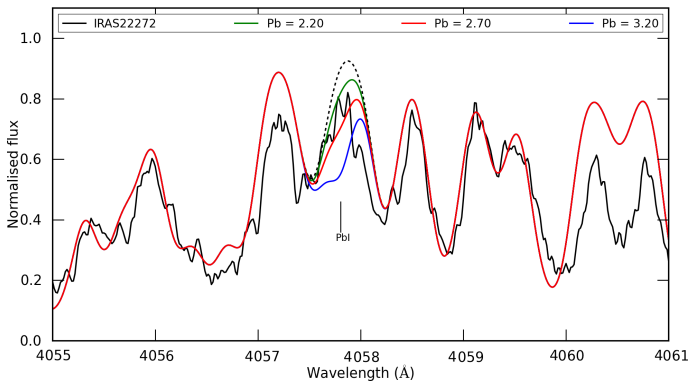


Fig. A.11. Spectrum synthesis of the Pb I line at 4057.807 Å for the HERMES spectrum of IRAS 22272+5435. Lines and symbols are similar to Fig. A.1.

A.11. We use the spectral blends at 4057.5 and 4058.8 Å to estimate the position of the continuum. We then adopt a Pb abundance upper limit that fully includes the visible line feature at 4057.807 Å.

The adopted $[\text{Pb}_{\text{up}}/\text{Fe}]$ of IRAS 22272+5435 lies between the results of $[\text{hs}/\text{Fe}]$ and $[\text{ls}/\text{Fe}]$ (right lower panel of Fig. 8). The element-over-iron ratios of the elements beyond the Ba-peak are also slightly higher than $[\text{Pb}_{\text{up}}/\text{Fe}]$.

Appendix B: Comparison to previous studies

In this appendix, we present the comparisons of our derived abundances with those of previous studies. In this paper we rely on high-quality data and perform strictly homogeneous abundance analyses based on the same methods and atomic data. The comparison with the literature is overall satisfactory but some noticeable differences occur, especially when the original data were of inferior quality to our UVES and Hermes data.

Objects IRAS 05113+1347 and IRAS 22272+5435 have been previously studied by Reddy et al. (2002); the comparisons between the abundance results are presented in Figs. B.1 and B.2. We find similar sets of atmospheric parameters although our derived metallicity for IRAS 05113+1347 is approximately 0.2 dex higher. We find a higher C/O ratio for IRAS 05113+1347 but lower abundances for Y and the heavy s-elements. In particular, Pr and Sm differ strongly, by almost 0.8 dex. For Sm, the same occurs with IRAS 22272+5435, for which Reddy et al. (2002) find an abundance that is about 1.25 dex higher than our Sm abundance. For all other elements, the abundance differences are significantly lower. Given the consistent distribution of the abundances presented here, and the superior S/N of our UVES spectra, we evaluate our new abundances to be more reliable.

For IRAS 05341+0852, IRAS 07134+1005, IRAS 19500-1709, and IRAS 22223+4327, we find similar atmospheric parameters as Van Winckel & Reyniers (2000). The strongest difference is the derived temperature of IRAS 05341+0852, which is 250 K hotter in our study. We find similar results for IRAS 05341+0852 (Fig. B.3) and IRAS 07134+1005 (Fig. B.4), and only our Sm result differs by about 0.4 dex from that of Van Winckel & Reyniers (2000). For IRAS 19500-1709 (Fig. B.5), all results are similar except for Nd and Eu, for which we find abundances that are a remarkable 0.9 dex higher. The large differences in those two elements are attributed to the use of a different set of spectral lines to determine the abundances. Van Winckel & Reyniers (2000) used only one very small line in the blue (λ 3863.408) with a measured EW \approx 3 mÅ to probe the

Nd abundance and also used a line of 3 mÅ for the Eu abundance. The analyses of Nd presented here is based on five lines with EWs ranging from about 5 up to 24 mÅ. We devised a much more systematic approach to our earlier work and find the low Nd abundance of our earlier work, Van Winckel & Reyniers (2000), to be suspicious given the very small and maybe spurious line. Also, in our new abundance of Eu presented here, the value is only based on one line; this is different than our earlier work with an EW \approx 16 mÅ.

Our abundance results of IRAS 22223+4327 (Fig. B.6) are similar to the determined abundances from Van Winckel & Reyniers (2000) and Rao et al. (2012). All three independent studies confirm the overabundance of ls elements with respect to the hs elements of IRAS 22223+4327.

Our atmospheric parameter results for IRAS 06530-0213 and IRAS 08143-4406 (Figs. B.7 and B.8) confirm the derived atmospheric parameter sets of Reyniers et al. (2004). Since only the combined $[\text{X}/\text{Fe}]$ results for the two observational settings for IRAS 08143-4406 are provided in Reyniers et al. (2004), we compare our individual results for the two settings with these combined results. For both stars, our results are similar. The strongest difference is our higher Zr abundance of about +0.3 dex with respect to Reyniers et al. (2004).

For IRAS 07430+1115 (Fig. B.9), we find large abundance differences with respect to Reddy et al. (1999) for almost all s-process elements, even though we used almost exactly the same atmospheric parameter set. Reddy et al. (1999) find Y and Zr abundances that are ± 0.5 and ± 1.0 dex higher than our results, respectively. Reddy et al. (1999) find lower abundances of about 0.3 dex for Sm and Eu. Except for one Eu line, we have used a different set of spectral lines than Reddy et al. (1999) for the analysis of Y, Zr, Sm, and Eu because many of these lines are part of a spectral blend in our UVES spectra. If these blends are included in the EW calculation, they result in EWs that are much higher than the actual EW, which may explain the difference between our abundance results and those of Reddy et al. (1999). For the only common Eu, we find a difference of -0.07 dex between our log gf value and those of Reddy et al. (1999), which may partly explain the abundance difference.

The atmospheric parameter results of Reyniers et al. (2007b) for IRAS 08281-4850 and IRAS 14325-6428 are similar to our results, although they find a microturbulent velocity, which is 4 km/s higher than our preferred result for IRAS 14325-6428. We find similar results for IRAS 08281-4850 (Fig. B.10) and also for IRAS 14325-6428, (Fig. B.11) despite the large microturbulence difference.

As discussed above, our results for IRAS 22223+4327 correspond to those of Rao et al. (2012). In case of IRAS 17279-1119 (Fig. B.12), we find similar atmospheric parameters as Rao et al. (2012) except for our log g, which differs by +1.0 dex from that of Rao et al. (2012). We find a stronger enrichment of the hs elements resulting in a mean $[\text{hs}/\text{Fe}]$ of about 0.9 dex, while Rao et al. (2012) find $[\text{hs}/\text{Fe}] \approx 0.6$ dex. Nevertheless, we still classify this object as mildly s-process enriched ($[\text{s}/\text{Fe}] < 1$) based on our abundance results.

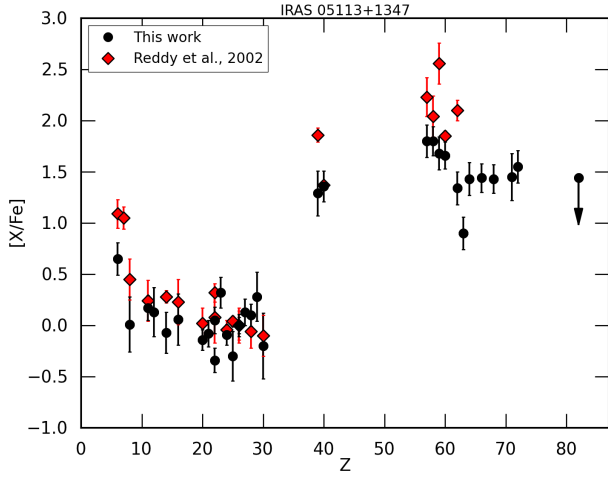


Fig. B.1. Comparison between our derived abundances and the results of Reddy et al. (2002) for IRAS 05113+1347.

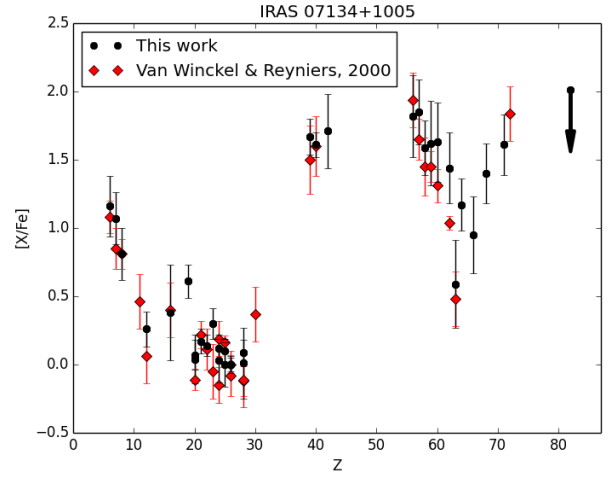


Fig. B.4. Comparison between our derived abundances and the results of Van Winckel & Reyniers (2000) for IRAS 07134+1005.

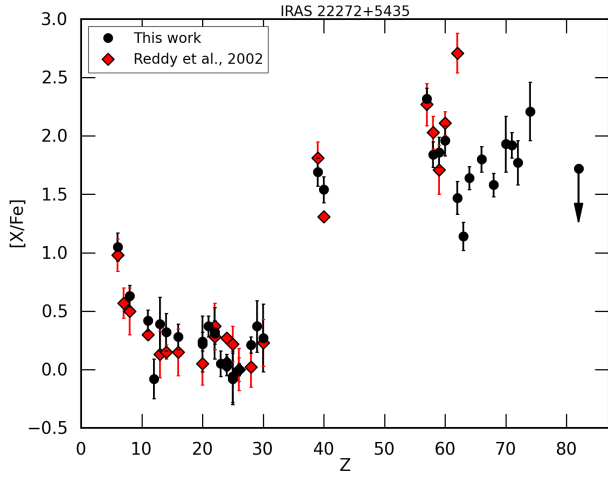


Fig. B.2. Comparison between our derived abundances and the results of Reddy et al. (2002) for IRAS 22272+5435.

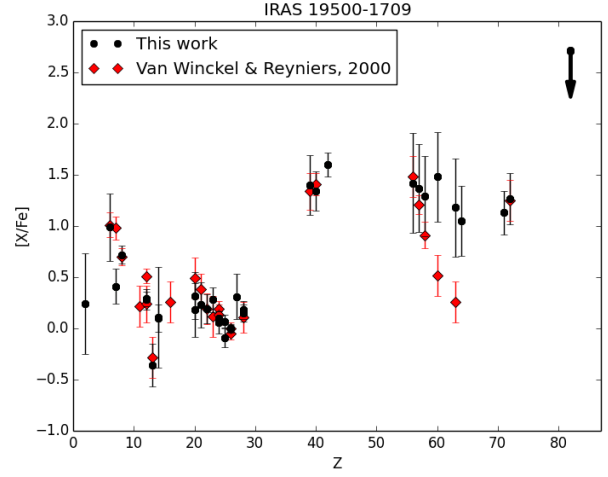


Fig. B.5. Comparison between our derived abundances and the results of Van Winckel & Reyniers (2000) for IRAS 19500-1709.

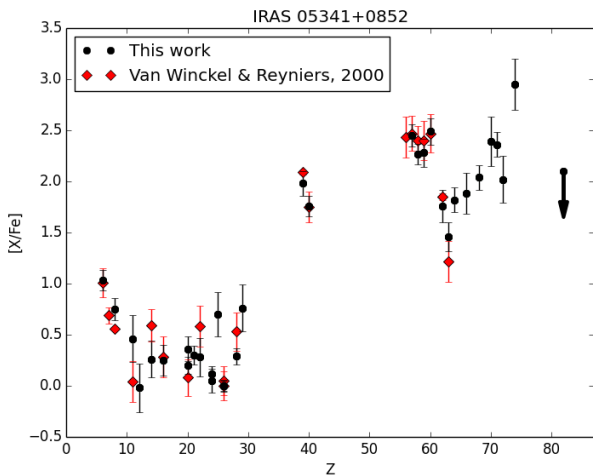


Fig. B.3. Comparison between our derived abundances and the results of Van Winckel & Reyniers (2000) for IRAS 05341+0852.

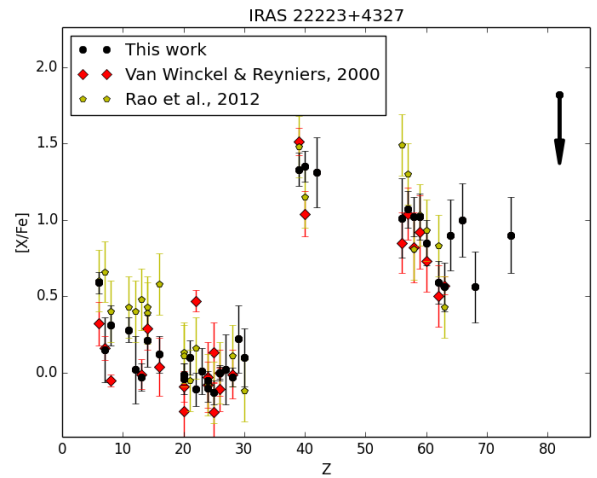


Fig. B.6. Comparison between our derived abundances and the results of Van Winckel & Reyniers (2000) and Rao et al. (2012) for IRAS 22223+4327. We adopt a standard deviation of 0.2 dex for all results of Rao et al. (2012).

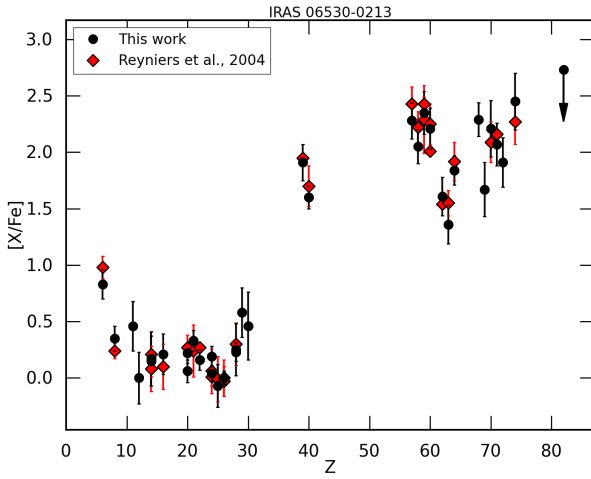


Fig. B.7. Comparison between our derived abundances and the results of Reyniers et al. (2004) for IRAS 06530-0213.

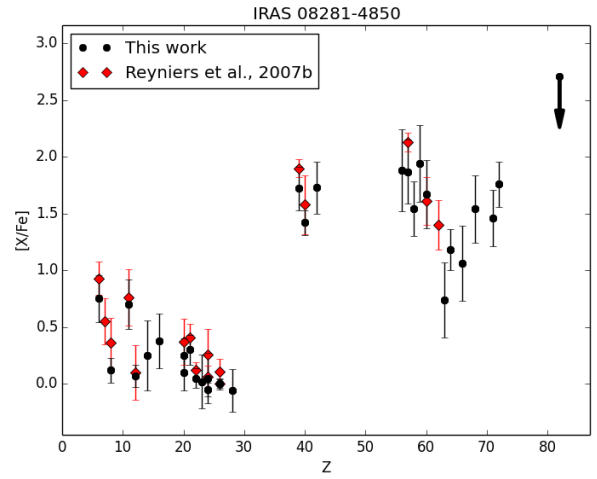


Fig. B.10. Comparison between our derived abundances for both observations of IRAS 08281-4850 and the final results of Reyniers et al. (2007b).

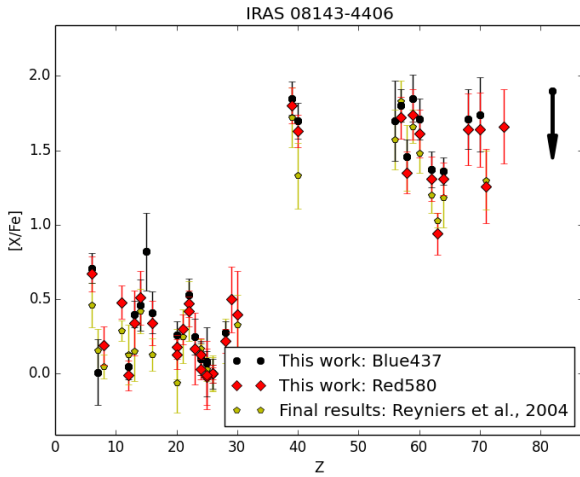


Fig. B.8. Comparison between our derived abundances for both observational settings of IRAS08143-4406 and the final results of Reyniers et al. (2004).

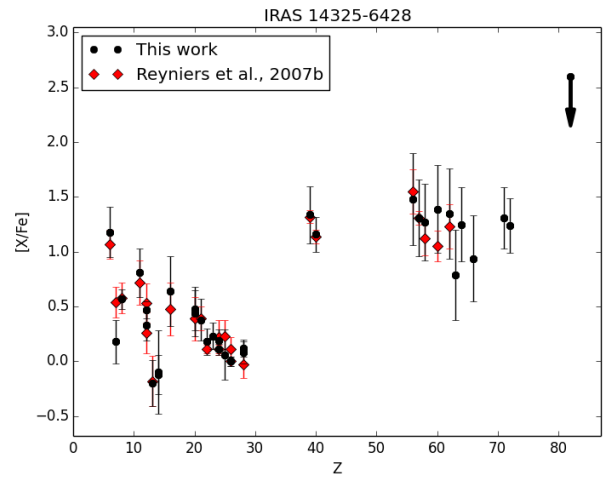


Fig. B.11. Comparison between our derived abundances for both observations of IRAS 14325-6428 and the final results of Reyniers et al. (2007b).

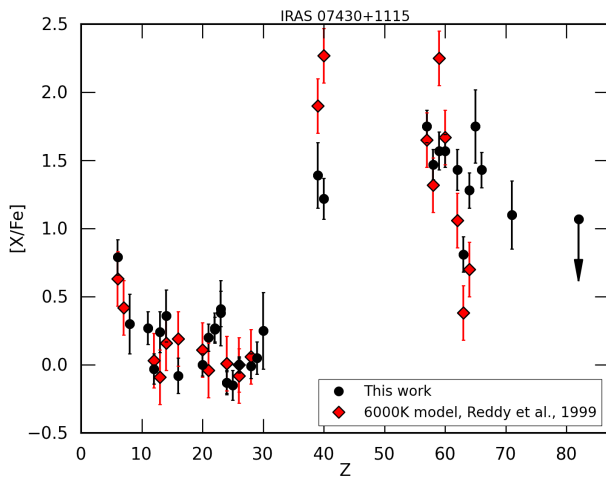


Fig. B.9. Comparison between our derived abundances and the results of Reddy et al. (1999) for IRAS 07430+1115. We adopt a standard deviation of 0.2 dex for all results of Reddy et al. (1999).

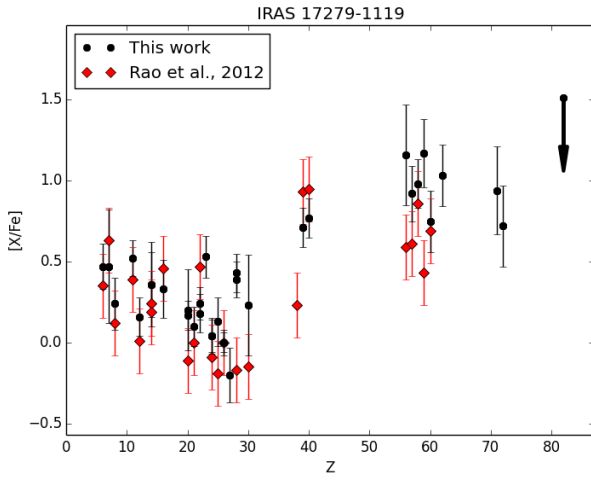


Fig. B.12. Comparison between our derived abundances and the results of Rao et al. (2012) for IRAS 17279-1119. We adopt a standard deviation of 0.2 dex for all results of Rao et al. (2012).